JGR Atmospheres

RESEARCH ARTICLE
10.1029/2019JD031266

Ensemble Sensitivity Analysis of Heavy Rainfall Associated With Three MCSs Coexisting Over Southern China

Yian Shen[1,2,3], Yu Du[1,2,3], and Guixing Chen[1,2,3]

[1]School of Atmospheric Sciences, and Guangdong Province Key Laboratory for Climate Change and Natural Disaster Studies, Sun Yat-sen University, Guangzhou, China, [2]Southern Marine Science and Engineering Guangdong Laboratory (Zhuhai), Zhuhai, China, [3]Guangdong Provincial Field Observation and Research Station for Climate Environment and Air Quality Change in the Pearl River Estuary, Guangzhou, China

Key Points:

- Ensemble sensitivity analysis indicates complex and different key factors contributing to rainfall related to three coexisting MCSs
- Two of the three MCSs are related to the shape of the vortex and the direction of LLJs, while the other MCS is linked to the strength of the SLLJ
- The forecast uncertainties of the vortex/shear line and low-level jets mainly contributed to the forecast uncertainty of the three MCSs

Correspondence to:
Y. Du,
duyu7@mail.sysu.edu.cn

Citation:
Shen, Y., Du, Y., & Chen, G. (2020). Ensemble sensitivity analysis of heavy rainfall associated with three MCSs coexisting over southern China. *Journal of Geophysical Research: Atmospheres*, *125*, e2019JD031266. https://doi.org/10.1029/2019JD031266

Received 2 JUL 2019
Accepted 19 DEC 2019
Accepted article online 23 DEC 2019

Abstract Using ensemble-based sensitivity analysis, a heavy rainfall event over southern China was analyzed to investigate the key controlling factors of rainfall amount and relevant predictability. The heavy rainfall event was caused by three coexisting mesoscale convective systems (MCSs) over southwestern China (MCS-A), the south coast of China (MCS-B), and northern Taiwan (MCS-C). The three MCSs exhibited differences and similarities with respect to their forecast accuracy and relevant key factors contributing to the rainfall centers, such as low-level vortex/shear lines and low-level jets. The strength and shape of the southwest vortex, a mesoscale vortex usually located over southwestern China with a horizontal scale of 200–600 km, exerted a significant effect on MCS-A and MCS-B, whereas the stronger shear line near the east coast of China was accompanied by increased precipitation in MCS-C. In addition, the low-level jets (LLJs) and their associated moisture transports had a strong influence on the three MCSs according to the LLJ location, strength, height, and direction. A synoptic LLJ located to the southeast of the southwest vortex with a stronger meridional (zonal) wind component and an axis more to the north (south) was related to increased precipitation in the corresponding region of MCS-A (MCS-B). In addition to the synoptic LLJ, the rainfall of MCS-B was also influenced by a boundary layer jet over the ocean. Uncertainties in the aforementioned key factors might further influence the predictability of the three MCSs and thus lead to the differences in their forecast accuracy.

1. Introduction

The presummer rainy season in South China is characterized by frequent long-duration heavy rainfall events from April to June, the first rainy season on the Chinese mainland, which contributes approximately half of the annual precipitation (Luo et al., 2017). Heavy rainfall during this rainy season may lead to severe floods or mudslides and thus cause large economic and human losses (Zhou et al., 2003). Organized mesoscale convective systems (MCSs) are regarded as a main contributor to heavy rainfall during the rainy season (Kuo & Chen, 1990; Luo et al., 2013; Zhang et al., 2003). Heavy rainfall and relevant MCSs during the presummer rainy season can be influenced by complicated multiscale atmospheric processes, including synoptic or subsynoptic weather systems (Huang et al., 2018; Kuo & Chen, 1990; Luo et al., 2016; Zhang et al., 2003; Zhang & Meng, 2018), local forcings such as terrain effects (Wang, Luo & Jou., 2014), land-sea breezes (Chen et al., 2015; Chen et al., 2016), boundary layer winds or jets (Du & Chen, 2019b), convectively generated cold pools (Liu et al., 2018; Wu & Luo, 2016), and urban heat islands (Wu et al., 2019).

Because of the complicated multiscale atmospheric processes involved, the skills of quantitative precipitation forecasting for heavy rainfall over southern China remain rather low for the models used at the National Meteorological Center of China (Luo et al., 2017). Accurately predicting the precise location, timing and amount of precipitation in South China during the presummer rainy season using global ensemble prediction systems also remains challenging (Huang & Luo, 2017). Huang and Luo et al. (2017) analyzed ensemble forecasts of four representative cases of torrential rainfall and demonstrated that the error in the quantitative precipitation forecast of heavy rainfall over southern China is closely related to the error in the predicted upstream low-level warm-moist southwesterly flow and moisture amount. Zhang and Meng (2018) documented that the uncertainty of the location of a low-level vortex could

significantly change the geopotential height uncertainty in the control area and further influence precipitation. Bei and Zhang (2007) explored the predictability of a warm-season heavy rainfall event along the Mei-Yu front of China and stressed the role of moist convection in the rapid error growth that leads to limited mesoscale predictability. Luo and Chen et al. (2015) also revealed that the forecast precipitation was strongly sensitive to uncertainties in the initial state, particularly for the initial moisture field. Zhang and Meng (2019) analyzed 45 warm-sector heavy rainfall episodes in southern China and demonstrated that WRF model simulations generally present lower quantitative precipitation forecasting skill associated with a low-level jet (LLJ; LLJ type) than in the no-LLJ type.

Ensemble-based sensitivity analysis (ESA; Hakim & Torn, 2008) has been widely used as an effective tool to explore key synoptic-scale factors of heavy rainfall events and their predictability. Zhang and Meng (2018) used ESA to examine the controlling factors of different rainfall stages in a persistent rainfall event and found that a LLJ was essential in that heavy rainfall event. Using a similar method, Du and Chen et al. (2018) further showed the different effects of the two types of LLJs on heavy rainfall, consisting of the synoptic-system-related low-level jet (SLLJ) in the low-level free troposphere and the boundary layer jet (BLJ) in the boundary layer with a strong vertical wind shear and diurnal cycle. Since multiple MCSs often coexist in South China, resulting in multiple rainfall centers, it is still not clear whether there are differences and similarities in the key factors contributing the development of coexisting MCSs in different regions under heavy rainfall events and whether there are correlations and interactions among the factors. In particular, it is necessary to examine the roles of the two types of LLJs in different MCSs.

The maximal daily rainfall over China during the presummer rainy season of 2015 occurred during an extreme heavy rainfall event with a maximum daily rainfall of 542 mm during 19–20 May 2015 over southern China (Wu & Luo, 2016). Three coexisting MCSs were observed during this rainfall event. Two MCSs were located in northeastern Guangxi Province and central Guangdong Province, which have a climate with a large amount of rainfall (Luo et al., 2017). Another MCS occurred over northern Taiwan and induced heavy rainfall, which was a typical heavy rainfall affected by the southeastward moving front system originating from Mainland China (Jing et al., 2004). The three MCSs might have responded differently to types of mesoscale forcing under the same synoptic background environment and might have interacted with each other, making accurate forecasts more difficult. Therefore, the key factors contributing the development of the three MCSs and relevant predictability are worth further study.

The objective of the current study is to reveal the differences and similarities in the roles of key controlling factors that affected the rainfall of different MCSs under the same synoptic background environment through ensemble-based sensitivity analysis. Section 2 introduces the data and methods used in this study, and section 3 provides an overview of the rainfall event. The differences in forecast accuracy among the ensemble forecasts are described in section 4. Section 5 presents the results of ensemble-based sensitivity analysis and composite analyses and further reveals the key factors in the three MCSs. Section 6 comprehensively presents the synoptic fields beneficial to all three MCSs. The predictability of the three MCSs is discussed in section 7. Finally, concluding remarks are given in section 8.

2. Data and Methods

The Climate Prediction Center morphing technique with a resolution of 30 min and 8 km was utilized for rainfall observation estimates in the present study. Climate Prediction Center morphing technique rainfall is derived from passive microwave data and half-hourly interval geostationary satellite infrared data (Joyce et al., 2004) and has been widely used to investigate heavy rainfall events (Catto et al., 2015; Monaghan et al., 2010) and diurnal variations in rainfall (Chen et al., 2016; Chen et al., 2018; Du & Rotunno, 2018).

ERA5 reanalysis data from the European Center for Medium-Range Weather Forecasts (ECMWF), with spatial and temporal resolutions of 0.25° and 1 hr, respectively, were utilized for synoptic environmental analyses in the present study. The ERA5 reanalysis data set is a global atmospheric reanalysis covering a period from 1979 onward that applies four-dimensional variational data assimilation. Since the global ensemble forecasts from ECMWF have a large ensemble size (containing 50 ensemble members) and well-tuned ensemble spread (Park et al., 2008), the ensemble forecasts from ECMWF, featuring a spatial resolution of 0.5°, temporal resolution of a 6-hr interval, and a 240-hr forecast period, were used to investigate the forecast capability and key factors of the three MCSs over southern China.

To examine the key factors contributing to heavy rainfall, ESA (Hakim & Torn, 2008) was adopted in the present study. After being introduced by Hakim and Torn (2008), ESA has been widely utilized to study heavy rainfall events (Huang & Luo, 2017; Lynch & Schumacher, 2014; Schumacher, 2011; Zhang & Meng, 2018) and estimate forecast sensitivities (Hill et al., 2016; Torn et al., 2017; Torn & Romine, 2015). ESA is a useful method to reveal the relative importance of various impact factors in rainfall events by calculating the magnitude of correlations between accumulated precipitation and weather variables. It should be noted that the ESA method has a hypothesis that the model can describe the dynamic and physical process of precipitation accurately and reasonably. To enlarge the ensemble sample size, two ensemble sets with different initial times of 0000 UTC 19 and 1200 UTC 19 May were combined into a larger ensemble set of 100 members in this study (Du & Chen, 2018; Zhang & Meng, 2018). The Pearson correlation coefficient was used to present the relation between the area-averaged 6-hr accumulated precipitation (0000–0600 UTC 20 May) in the three MCS regions and various weather variables at 0000 UTC 20 May. The Pearson correlation coefficient was calculated as follows:

$$r = \frac{\sum_{i=1}^{n}\left(X_i-\overline{X}\right)\left(P_i-\overline{P}\right)}{\sqrt{\sum_{i=1}^{n}\left(X_i-\overline{X}\right)^2\sum_{i=1}^{n}\left(P_i-\overline{P}\right)^2}}$$

where P represents the area-averaged 6-hr accumulated precipitation, X is a type of variable at a certain grid point, and n is the ensemble size (100) in the present study. Under a two-tailed significance test, assuming that the 100 members had an equal probability, correlations with magnitudes greater than 0.2 were significantly different from zero at the 95% confidence level. We also carried out separate analyses of each initialized ensemble containing 50 members. In addition, the threat score (TS) of heavy rain with a 25-mm threshold (Schaefer, 1990; Wang, 2014) was used to measure the forecast skill of the three MCSs. Composite analyses of good and bad members were conducted to further confirm the effects of key factors on rainfall forecast. Good and bad members, defined as the members with the most and the least accurate rainfall forecast, were chosen based on the rainfall amount and TSs for each MCS rainfall (Yu & Meng, 2016; Zhu & Xue, 2016) rather than other mesoscale environmental features, since three-dimensional multiple atmospheric variables involved make it practically difficult to do that. A good member could be good for one MCS but not good for neighboring MCSs. The specific members varied with the different MCSs, and ESA was utilized to analyze the three MCSs. Under this circumstance, the key factors and mesoscale features in composite fields of good members beneficial to one MCS might not be beneficial to another MCS. To comprehensively present the synoptic fields beneficial to all three MCSs, we also selected good and bad members for all three MCSs and conducted ensemble-based sensitivity or composite analysis for the three MCSs, as described in section 6.

3. Overview of the Rainfall Event

On 19–20 May 2015, a persistent heavy rainfall event occurred over southern China and other places (Figures 1 and 2). A rain band was located over southern China and gradually moved southeastward after 1900 UTC 19 May (Figures 1c, 1d, and 2a–2f). Then, the rain band broke into two MCSs, which were located in northeastern Guangxi Province and central Guangdong Province at 0000 UTC 20 May (Figures 1e, 1f, and 2g–2l). Another rainfall center was initiated over the Taiwan Strait at approximately 1900 UTC 19 May (Figure 2a). Then, the rainfall center moved to northern Taiwan island after 0000 UTC 20 May (Figures 2g–2l). Therefore, three strong precipitation centers existed simultaneously during 0000–0600 UTC 20 May (Figures 1d–1g and 2g–2l), corresponding to three mesoscale convective systems located in northeastern Guangxi Province (MCS-A), central Guangdong Province (MCS-B), and northern Taiwan (MCS-C; circled in Figure 1f).

Since the three MCSs might have different features and key factors that contribute to the heavy rainfall, the rainfall stages of the three MCSs during 0000–0600 UTC 20 May were selected as a case of interest in the present study. The distribution of accumulated precipitation during this period from Climate Prediction Center morphing technique indicated that the maximum rainfall values of MCS-A, MCS-B, and MCS-C were 69.1, 114.4, and 137.1 mm, respectively (Figure 3).

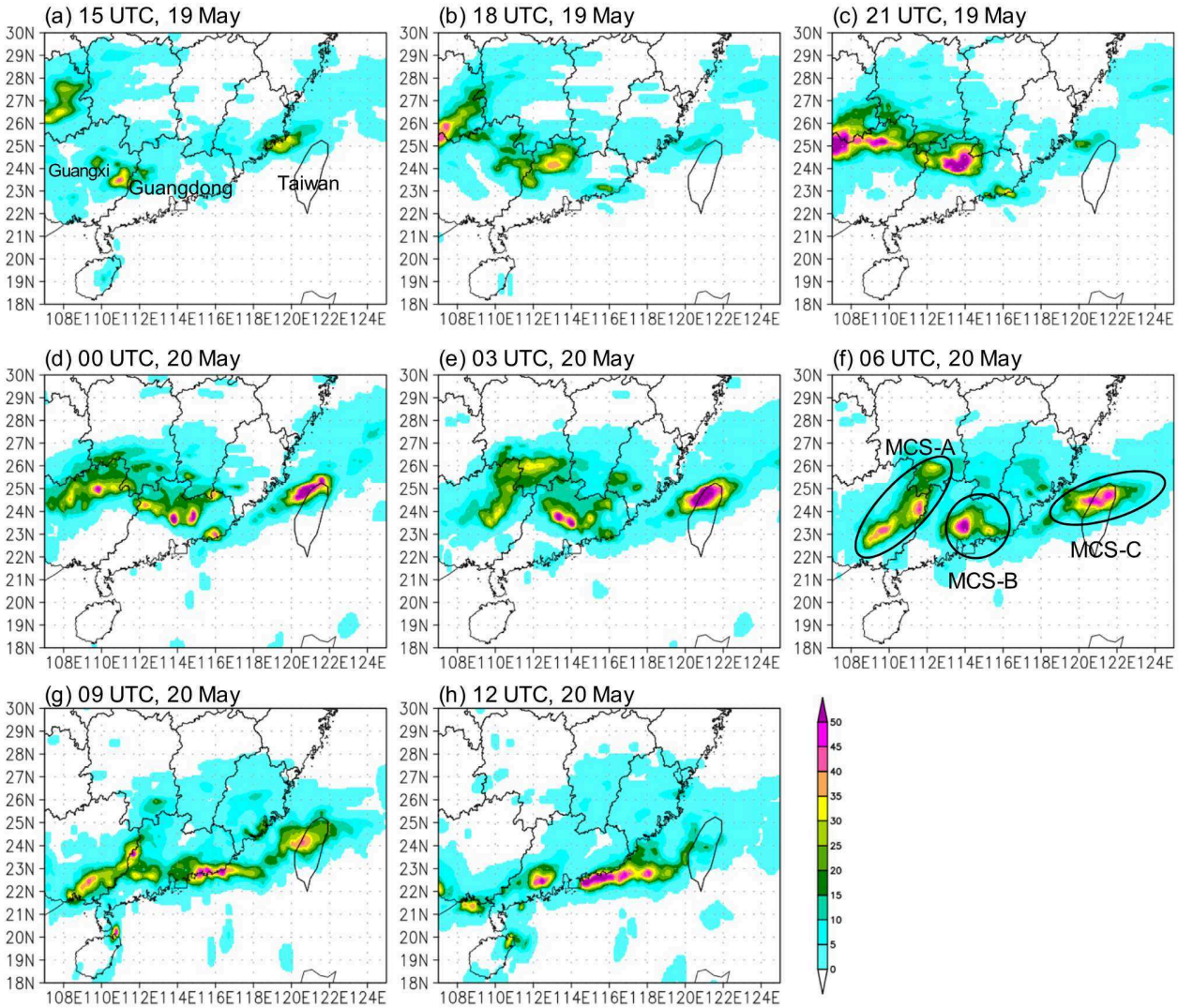

Figure 1. (a–h) Distribution of 3-hr accumulated precipitation from 1500 UTC, 19 May to 1200 UTC, 20 May 2015 using the CMORPH data. The locations mentioned in section 3 and the three MCSs are marked in (a) and (f).

Figure 4 shows the synoptic background environment during the present heavy rainfall event. At the 500-hPa level, there was a trough (marked by a solid red line in Figures 4a and 4b) in the midlatitude region. A west-east oriented shear line at 850 hPa occurred at approximately 25°N (black dashed line in Figure 4) and arose from cold advection from the East Asia trough and warm and humid airflow from the ocean. Along the shear line, a southwest vortex, which is defined as a mesoscale vortex usually located over southwestern China with a horizontal scale of 200–600 km, was generated over northwest Guangxi Province (Figure 4c). The precipitable water vapor was high in a large area of southern China and gradually increased from 1800 UTC 19 to 0000 UTC 20 May (Figures 4a and 4b). Three low-level jets existed at the same time (marked by red circles in Figures 4c and 4d), transporting sufficient moisture to southern China.

4. Ensemble Forecasts

ECMWF ensemble forecasts exhibited varying capability in forecasting the MCSs. The forecast accuracy of the three MCSs was sensitive to the forecast initial time (Figures 5a–5c). The ensemble mean forecasts initiated at 0000 UTC 19 May almost missed MCS-B (Figure 5a) but captured the existence of MCS-A and MCS-C. MCS-B was captured by the ensemble mean forecasts initiated at 1200 UTC 19 May, but the

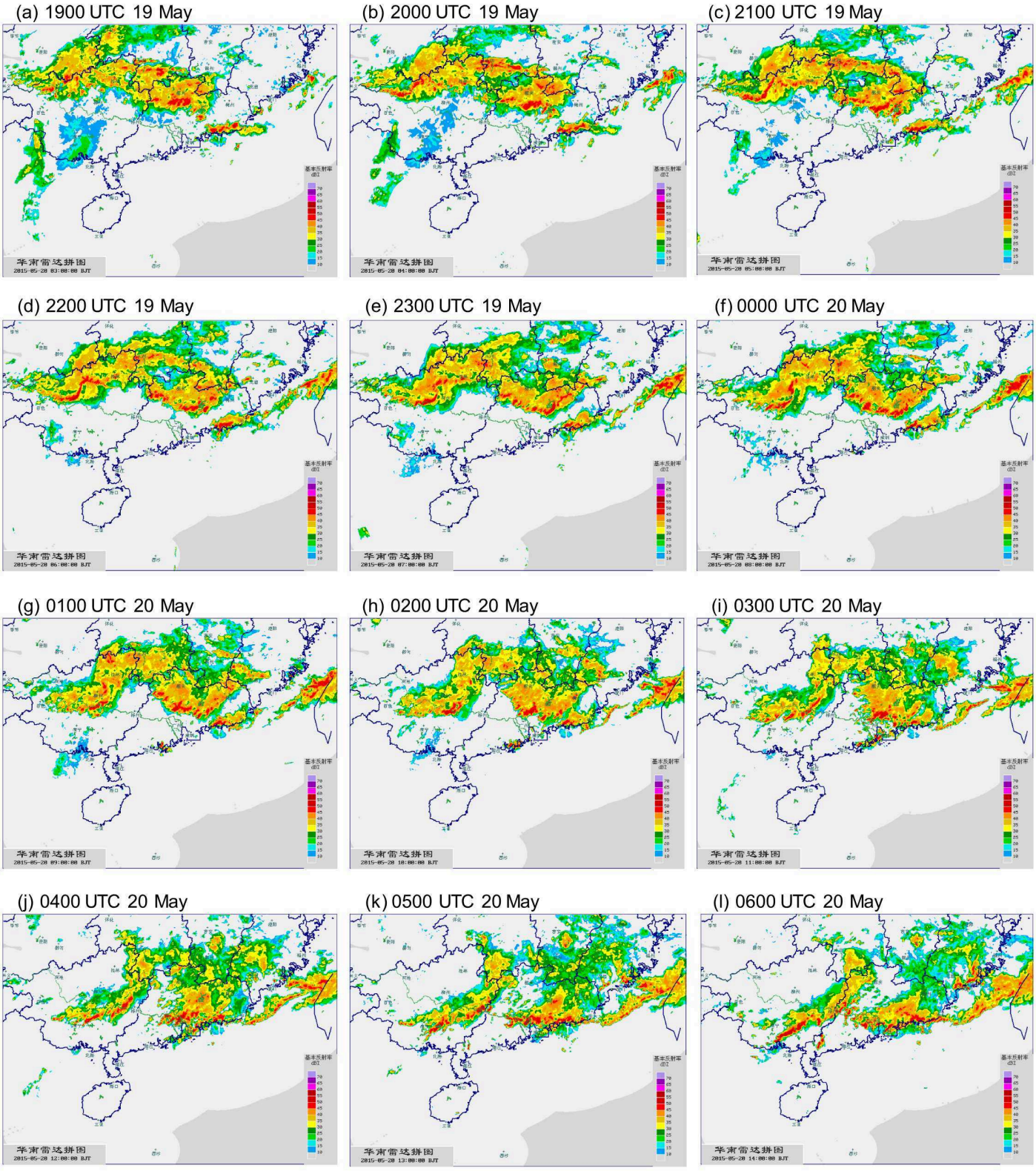

Figure 2. Radar composite reflectivity from (a) 1900 UTC 19 May 2015 to (l) 0600 UTC 20 May.

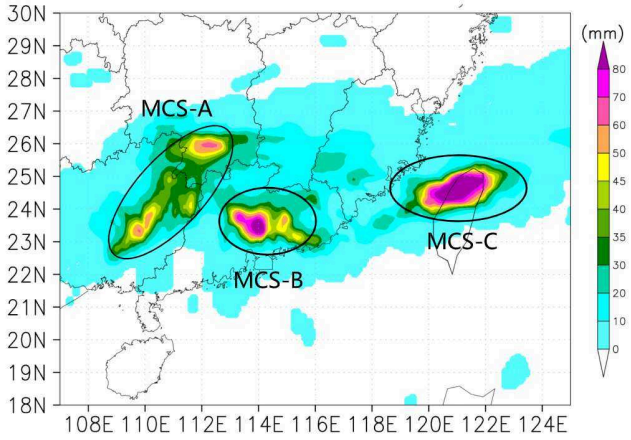

Figure 3. The 6-hr accumulated precipitation (shading; mm) during 0000–0600 UTC 20 May 2015 from the CMORPH data. The locations of three MCSs are marked by black circles.

forecast rainfall of MCS-A tended to be small, with a 6-hr accumulated precipitation less than 25 mm (Figure 5b). All ensemble forecasts with different initial times could forecast the precipitation in the control area of MCS-C, although the forecast rainfall tended to be northwest of the observed rainfall center (Figures 3, 5a, and 5b). The location errors in the forecast rainfall of the three MCSs were mainly caused by a misrepresentation of the MCS propagation within the ensemble forecast. For example, MCS-C was initiated over Taiwan Strait and gradually moved to northern Taiwan island after 0000 UTC 20 May, according to observations (Figures 2g–2l), but the forecast MCS-C was still located over Taiwan Strait during 0000–0600 UTC 20 May. Since these MCSs moved with time, the ensemble forecasts had a large spread and errors in the location and pattern of rainfall, which largely influenced the ESA and had a dominant effect on the relevant results. Therefore, in the present study, we focused more on the occurrence and overall magnitude of heavy rainfall centers than their detailed locations and patterns. In this way, the control areas of the three MCSs we chose (the black boxes in Figure 5) were generally based on both observation and forecast precipitation and were large enough to basically smooth out the location and pattern errors (Bednarczyk & Ancell, 2015).

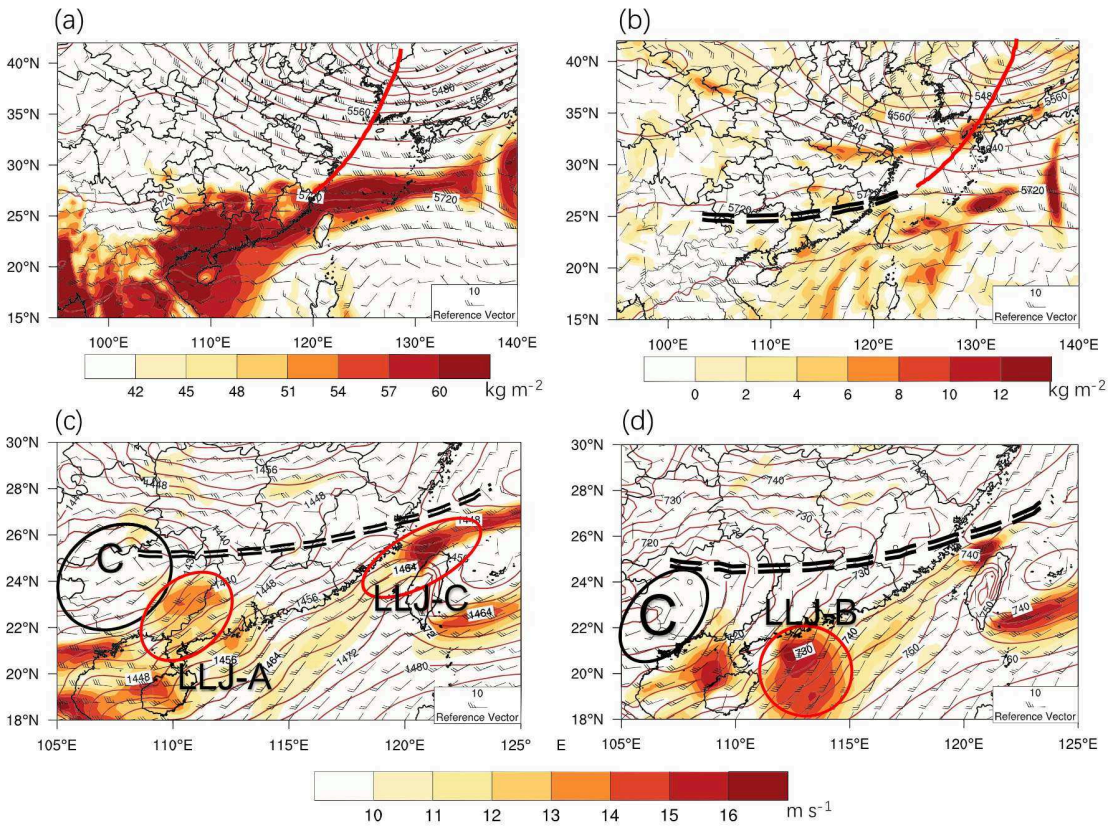

Figure 4. Synoptic background environment during the heavy rainfall event from the ERA5 reanalysis data set. (a) The 500-hPa geopotential height (contour; gpm), 500-hPa horizontal wind barb and precipitable water (shading; kg m^{-2}) at 1800 UTC 19 May 2015; (b) 500-hPa geopotential height (contour; gpm), 850-hPa horizontal wind barb at 0000 UTC 20 May 2015, and the difference in precipitable water between 1800 UTC 19 and 0000 UTC 20 (shading; kg m^{-2}); the geopotential height (contour; gpm) and wind barb and wind speed (shaded over 10 m s^{-1}) at 0000 UTC 20 May 2015 at (c) 850 hPa and (d) 925 hPa. The troughs and shear lines are marked by solid red lines and black dashed lines, respectively. Black and red circles represent the vortex and LLJs, respectively.

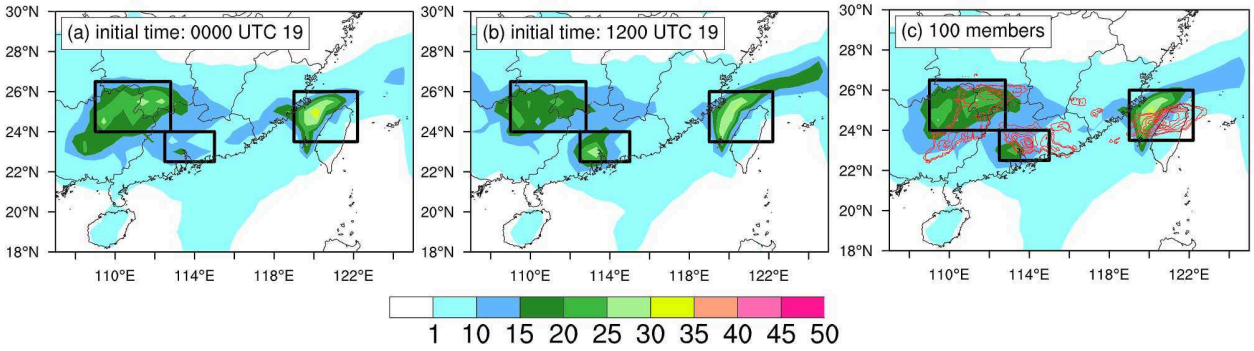

Figure 5. The 6-hr accumulated precipitation of ensemble forecasts with initial times of (a) 0000 UTC 19 May, (b) 1200 UTC 19 May, and (c) 100 members (shading; mm) and 6-hr accumulated precipitation from the CMORPH data (contours).

The histogram distributions of ensemble rainfall forecasts for the three MCSs are shown in Figures 6a–6c. Note that the rainfall amount of the three MCSs is averaged over the regions denoted by black boxes in Figure 5. The spread of the area-averaged precipitation of the two ensemble sets initiated from 00*Z* 19 May and 12*Z* 19 May (not shown), and the new ensemble set of 100 members (Figures 6a–6c) generally follows a Gamma distribution. The forecast precipitation amounts of the three MCSs (the average values of 100 members are marked by vertical solid lines) were all apparently underestimated compared to the observations (red dashed lines), which might be partly due to the coarse resolution of the global ensemble forecasts (Gopalakrishnan et al., 2011; Kumar et al., 2015). Nevertheless, the magnitude error of the area-averaged rainfall of MCS-A was smaller than that of MCS-B and MCS-C in the ensemble forecasts. The observed area-averaged 6-hr accumulated precipitation of MCS-A was 25.1 mm, while the ensemble mean of the forecast precipitation amounted to 16.24 mm (red solid line in Figure 6a). Note that several members yielded a forecast close to the observation for the precipitation of MCS-A. For MCS-B and MCS-C, the ensemble mean of the forecast precipitation (12.68, 14.31 mm) was only approximately half of the observed precipitation (33.3, 34.5 mm). A detailed check suggests that the causes of the forecast error of MCS-B and MCS-C were different. Some ensemble members missed the occurrence of MCS-B, while all members captured the occurrence of MCS-C but tended to underestimate its rain intensity. Although all ensemble members underestimated MCS-C, the ensemble spread was relatively small compared to that of MCS-A and MCS-B. The TSs for 25-mm thresholds of individual ensemble members of the three MSCs were conducted to evaluate the forecast skills (Figures 6d–6f). The ensemble members initialized at 0000 UTC 19 May and 1200 UTC 19 May are marked by "plus sign" and "cross," respectively (Figures 6d–6f). It is clear that most ensemble members with high TSs in MCS-B were initialized at 1200 UTC 19 May, while most members with high threat scores in MCS-A were initialized at 0000 UTC 19 May. For MCS-C, the number of members with high TSs initialized at 0000 UTC 19 May was approximately the same as that with high TSs initialized at 1200 UTC 19 May. The value of the ensemble mean TS of MCS-A and MCS-C was approximately 0.2, and the ensemble mean TS of MCS-B was only 0.1. In general, the forecast skill of MCS-B was the worst among the three MCSs. Since the TSs of MCS-A and MCS-B are positively correlated with area-averaged forecast precipitation (Figures 6d and 6e), ensemble members with the most accurate and inaccurate precipitation amounts for MCS-A and MCS-B were selected based on the area-averaged forecast precipitation. For MCS-A, six members (#1, 6, 21, 25, 28, and 67) were chosen as good members (red dots in Figure 6d), whereas the other six members (#22, 39, 61, 80, 85, and 90) were chosen as bad members (blue dots in Figure 6d). For MCS-B, good members were #2, 52, 56, 73, 80, and 98, and bad members were #18, 23, 30, 49, 50, and 60 (Figure 6e). As shown in Figure 6f, the positive correlation between the TS and area-averaged forecast precipitation was weaker for MCS-C than for MCS-A and MCS-B. In this way, the most accurate and inaccurate precipitation amounts of MCS-C were selected based on the combination of TSs and area-averaged precipitation. Good members of MCS-C were #5, 30, 31, 65, 68, and 79, and bad members were #21, 28, 29, 69, 76, and 97. The average rainfall distributions of good and bad members for the three MCSs are shown in Figure 7. For MCS-A, the precipitation values of good members were close to the observations in terms of the location and intensity (Figure 7a). In contrast, the rainfall in bad members

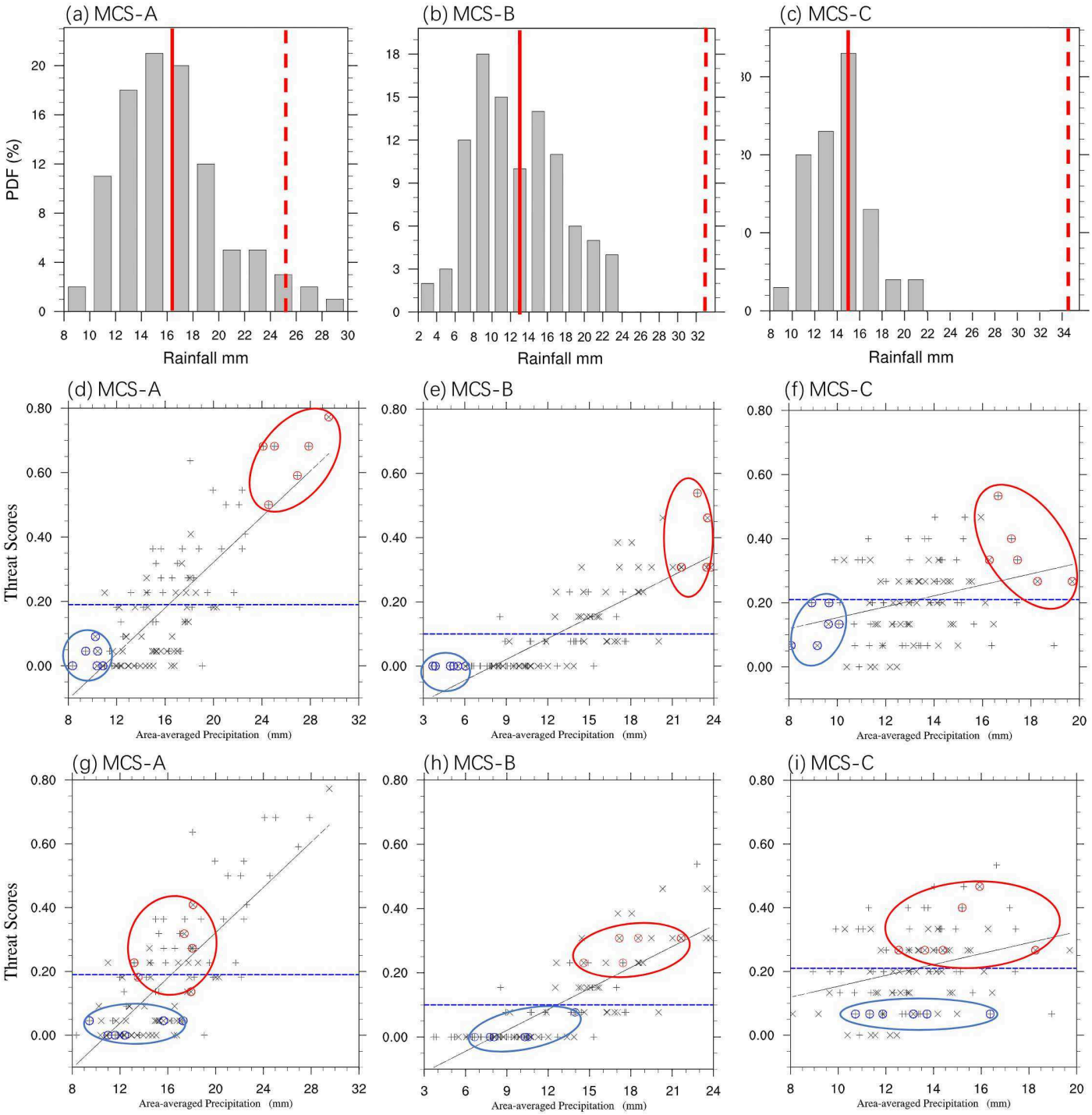

Figure 6. Histogram distribution of area-averaged precipitation during 0000–0600 UTC 20 May in (a) MSC-A, (b) MCS-B, and (c) MCS-C from the ECWMF ensemble forecasts. Ensemble means and corresponding observations of the area-averaged 6-hr accumulated precipitation are indicated by red vertical solid lines and dashed lines. The TSs of (d and g) MCS-A, (e and h) MCS-B, and (f and i) MCS-C, with (d–f) good and bad members for each MCS marked by red dots and blue dots, respectively, and (g–i) good and bad members for all three MCSs marked by red dots and blue dots. In each plot, the blue dashed line indicates the value of the ensemble mean TS. The ensemble members initialized at 0000 UTC 19 May are marked by "plus sign," and the ensemble members initialized at 1200 UTC 19 May are marked by "cross."

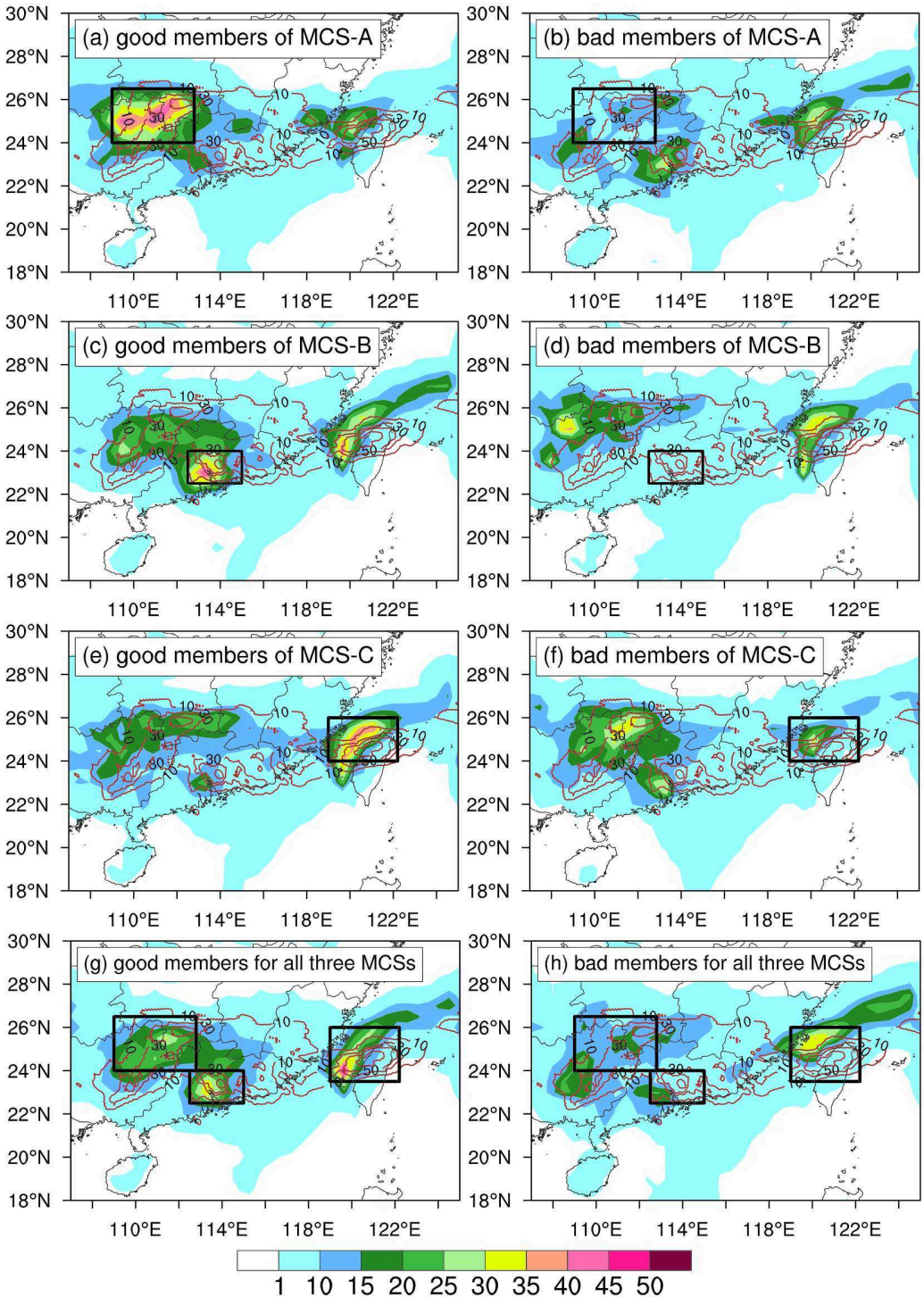

Figure 7. Composite fields of (a, c, e, and g) good members and (b, d, f, and h) bad members approximately 6-hr accumulated precipitation of (a and b) MCS-A, (c and d) MCS-B, (e and f) MCS-C, and for (g and h) all three MCSs, overlaid with 10-, 30-, 50-, and 90-mm contours of 6-hr accumulated precipitation from the CMORPH data.

was located to the south, out of the control region (denoted by the black box), with a much smaller rainfall amount (Figure 7b). Good members of MCS-B predicted a rainfall distribution similar to the observed distribution (Figure 7c), while bad members almost missed the rainfall center (Figure 7d). Both good and

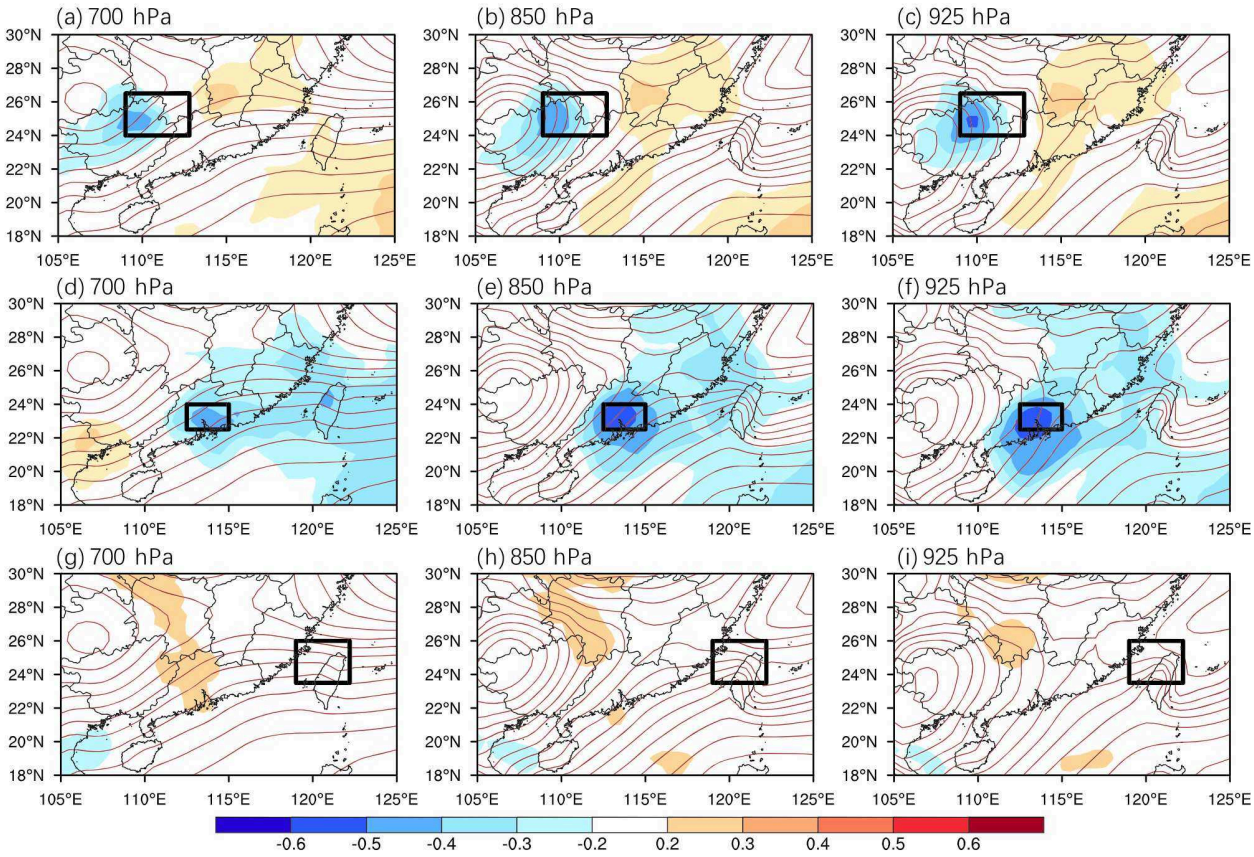

Figure 8. Correlation coefficients (shading) between geopotential height at (a, d, and g) 700 hPa, (b, e, and h) 850 hPa, and (c, f, and i) 925 hPa at 0000 UTC 20 May and 6-hr area-averaged accumulated precipitation of (a–c) MCS-A, (d–f) MCS-B, and (g–i) MCS-C during 0000–0600 UTC 20 May. The ensemble mean geopotential height fields are plotted as contours.

bad members could roughly capture the location of MCS-C, but the rainfall of bad members was apparently weaker than that of good members (Figures 7e and 7f).

5. Key Factors Influencing Three Coexisting MCSs

To reveal the key factors that contribute to the forecast rainfall associated with three coexisting MCSs, ensemble-based sensitivity analysis was applied by examining the relationship between the relevant variables at 0000 UTC 20 May and the subsequent 6-hr accumulated precipitation during 0000–0600 UTC 20 May in the three MCSs. Composite fields of the good and bad members were further constructed to confirm the influence of those key factors.

5.1. Low-Level Vortices/Shear and Troughs

The distribution of the correlation coefficients between the precipitation of the three MCSs and the geopotential height of 100 ensemble forecast members is presented in Figure 8. Significant negative correlation signals occurred in the control area of MCS-A, with maximum coefficients of −0.51 at 925 hPa, −0.48 at 850 hPa, and −0.44 at 700 hPa (Figures 8a–8c). This indicates that the decreased geopotential heights in the control region at low levels were related to the increased precipitation of MCS-A. Furthermore, significant positive correlation signals occurred in the east of the control area. A dipole pattern of positive and negative coefficients was correlated with the position of the relevant synoptic systems (Bednarczyk & Ancell, 2015). Similar to MCS-A, negative correlation coefficients also occurred near the center of MCS-B; however, the negative correlation was most apparent at 925 hPa, with a maximum coefficient of −0.60, and significantly deceased with height in MCS-B (Figures 8d–8f). This suggests that MCS-B was more sensitive to

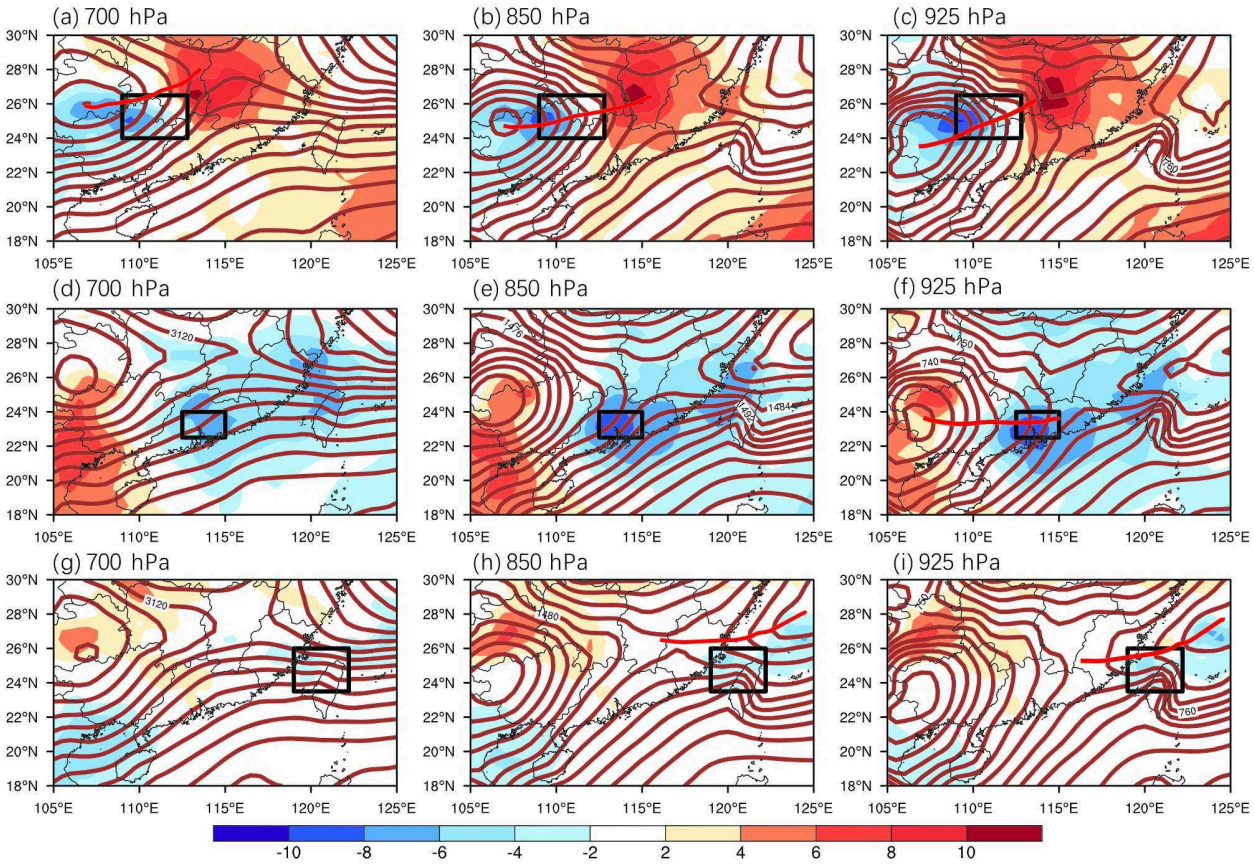

Figure 9. The geopotential heights of good members (contour lines; gpm) and the differences in geopotential heights (shading; gpm) at (a, d, and g) 700 hPa, (b, e, and h) 850 hPa, and (c, f, and i) 925 hPa between good members and bad members of (a–c) MCS-A, (d–f) MCS-B, and (g–i) MCS-C. The troughs of the vortices and shear lines are marked by red lines.

the geopotential height at 925 hPa than at 850 and 700 hPa. A reverse dipole pattern with a negative correlation over the east and a positive correlation over the west occurred at 700 hPa. In contrast to MCS-A and MCS-B, there was no significant correlation in the control area of MCS-C (Figures 8g–8i).

To further confirm the impact of geopotential height on rainfall, the differences in geopotential height between good and bad members were determined and are shown in Figure 9. For good members of MCS-A, there was a northeast-southwest oriented trough at low levels in the control area, and the geopotential height in the control area was approximately 8 geopotential meters lower for good members than for bad members at all low levels (925–700 hPa; Figures 9a–9c). In agreement with the ESA results described above, the lower geopotential height at 0000 UTC 20 May in the control area was related to more precipitation in MCS-A during 0000–0600 UTC 20. Similarly, good members of MCS-B showed a northwest-southeast oriented trough in the control area at 925 hPa, which differs from the results of MCS-A (Figures 9d–9f). The negative differences in the geopotential height of good and bad members reached −9.79 geopotential meters at 925 hPa but decreased with height in the control area, which was also consistent with the ESA results. This result reinforces that the strength and orientation of the low-level trough related to the southwest vortex in the control area were crucial to the precipitation forecast of MCS-A and MCS-B. The precipitation of MCS-B was mainly influenced by the geopotential height at 925 hPa, whereas the precipitation of MCS-A was sensitive at all low levels (925–700 hPa). Similar to the dipole correlation patterns, MCS-A and MCS-B had opposite dipole patterns of positive and negative differences. These opposite dipole patterns indicated that an amplification of the trough over the MCS-A region is related to increased precipitation for MCS-A, while an amplification of the trough over the MCS-B region and deamplification of the southwest vortex is correlated with increased precipitation for MCS-B. As mentioned in section 4 in the manuscript,

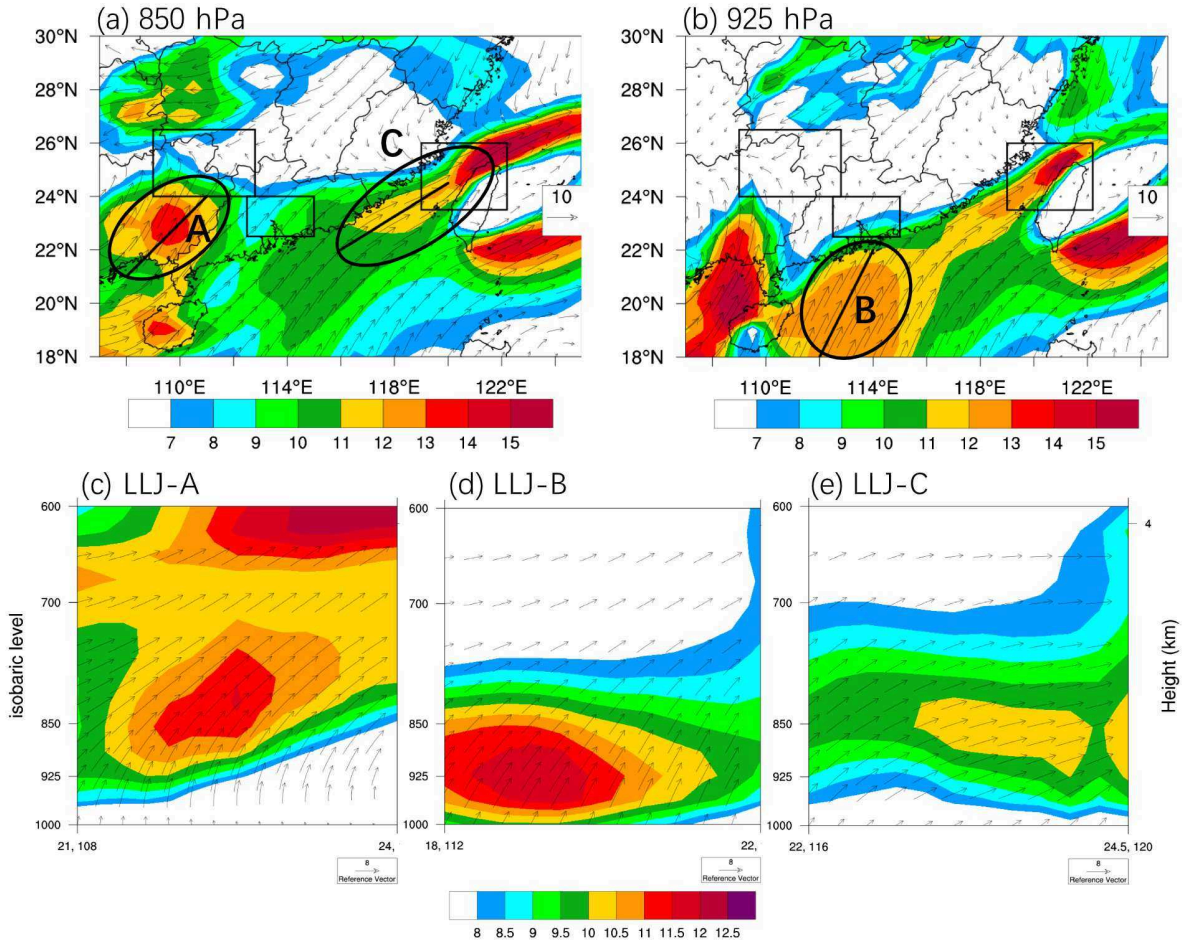

Figure 10. Winds of ensemble mean forecast (shading; m s^{-1}) at (a) 850 hPa and (b) 925 hPa. Black circles in Figures 10a and 10b represent the locations of the low-level jets. Vertical cross sections of three low-level jets from ERA5 analysis data along the black lines in (a) and (b) are shown in (c)–(e). The changes in the horizontal wind vector with height are shown in (c)–(e), with upward vectors indicating the direction toward the north.

the forecast accuracy of MCS-B is opposite to that of MCS-A (Figure 5). The opposite dipole patterns are correlated with the opposite relationship between the forecast precipitation of MCS-A and MCS-B. According to the geopotential height in good members of MCS-C, a strong shear line located over the east coast of China was related to increased precipitation in MCS-C (Figures 9g–9i). The detailed effect of the shear line is discussed in section 5.2.

5.2. Low-Level Jets

In the present rainfall event, there were three low-level jets (LLJ-A, LLJ-B, and LLJ-C marked by black circles in Figure 10) that were related to the three MCSs. LLJ-A and LLJ-C, with cores at 850–700 hPa, were located in the area adjacent to the corresponding MCSs (Figure 10a). LLJs can be classified into two types: SLLJs, which occur in the low-level free troposphere, and BLJs, which occur in the boundary layer and have strong vertical wind shear and a diurnal cycle (Du et al., 2012; 2014). The SLLJs are in close association with synoptic-scale weather systems, while the BLJs are mainly caused by boundary processes such as inertial oscillations (Blackadar, 1957; Blackadar mechanism) and thermal contrast near the terrain or coastal areas (Holton, 1967; Holton mechanism) (Du & Rotunno, 2014). BLJs can also be modulated by synoptic disturbances. Since the LLJ-A and LLJ-C in this study were located to the southeast of the southwest vortex or the south of the low-level shear line, respectively, and their location and direction were closely related to the vortex/shear, they were classified as SLLJs. In addition, LLJ-B was a boundary layer jet at 925 hPa that was located to the south of MCS-B (Figure 10b). The distinctions among the heights of three low-level jets were further confirmed by the vertical cross sections of three low-level jets (Figures 10c–10e). LLJ-A and

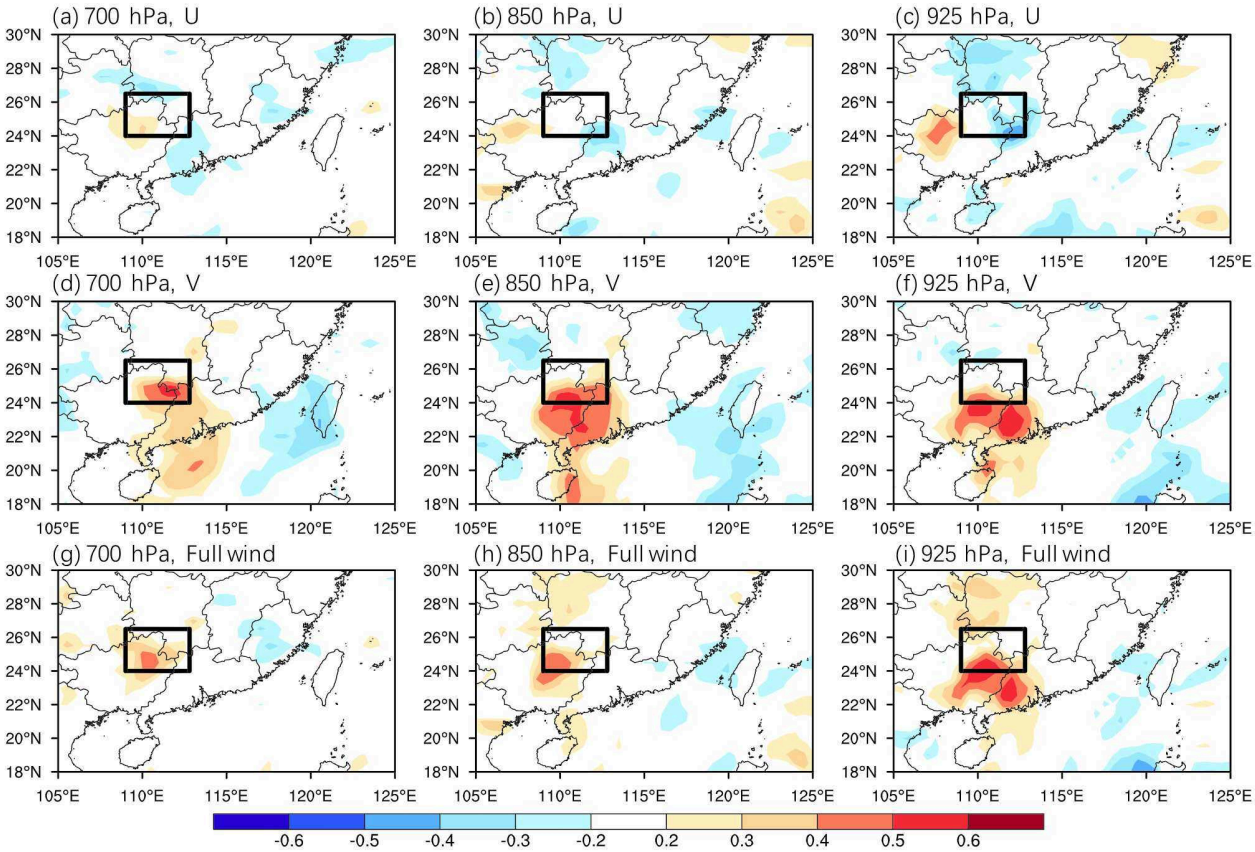

Figure 11. Correlation of (a–c) zonal wind velocity, (d–f) meridional wind velocity, and (g–i) full wind velocity at (a, d, and g) 700 hPa, (b, e, and h) 850 hPa, and (c, f, and i) 925 hPa at 0000 UTC 20 May with area-averaged precipitation of MCS-A during 0000–0600 UTC 20 May.

LLJ-C presented maximum wind speeds at 850–700 hPa, with relatively low wind speeds at 925 hPa. The core of LLJ-B was observed at 925 hPa, while the wind speed at 850–700 hPa was apparently less than 10.5 m s^{-1}. As described in this section, the influence of these three low-level jets was examined by calculating the correlations between winds (including meridional wind velocity, zonal wind velocity, and full wind velocity) and precipitation.

As shown in Figures 11a–11c, weak positive correlations between the zonal wind velocity and accumulated precipitation of MCS-A occurred west of the control area at 925–700 hPa, indicating that an increase in the zonal wind strength over the southwest of the control area was correlated with more precipitation. Meanwhile, negative signals were observed over the north and east of the control area, indicating that a stronger convergence occurred there. Similar results were presented by the correlation between meridional wind velocity and accumulated precipitation (Figures 11d–11f). A strong positive signal over the south of the control area ($r \approx 0.6$) and a weak negative signal over the north of the control area at 925–850 hPa suggest that increases in the meridional wind strength over the south of the control area and convergence were correlated with increased precipitation. Negative correlations also occurred near the Taiwan Strait, indicating that SLLJ maintained upstream rather than downstream movement, which was correlated with increased precipitation of MCS-A. For the correlation coefficients between the full wind velocity and accumulated precipitation of MCS-A, a strong positive region and a weak positive region occurred over the south and north of the control area, respectively (Figures 11g–11i). This implies that a stronger upstream SLLJ with stronger meridional and northerly winds over the north of the control area was correlated with increased precipitation in MCS-A (Du & Chen, 2018).

The composite full wind speed fields of good and bad members are compared in Figure 12. The good members forecasted a stronger low-level jet than the bad members, with a maximum wind speed over 14 m s^{-1}.

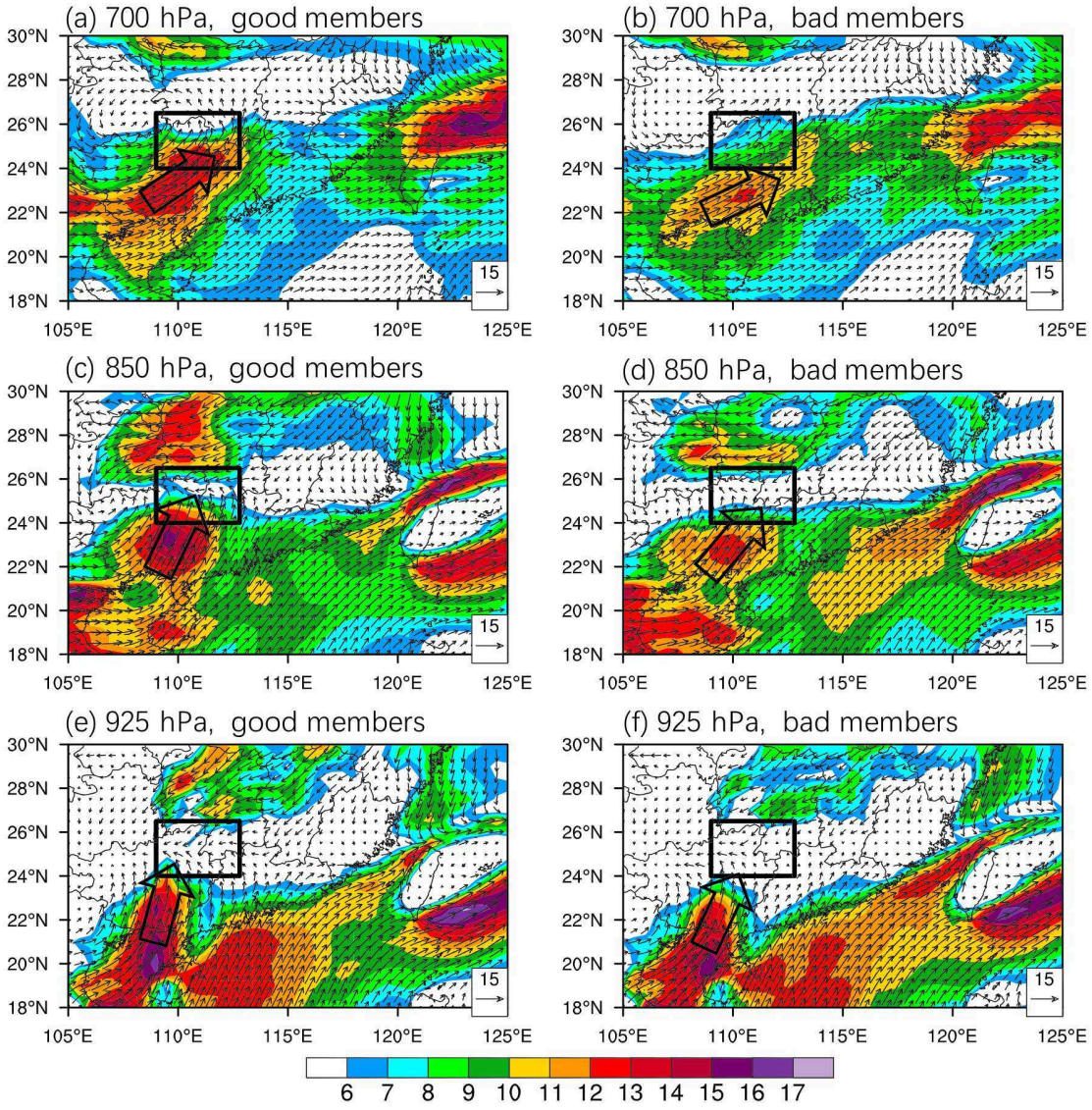

Figure 12. Composite wind fields of (a, c, and e) good members and (b, d, and f) bad members of MCS-A with full wind speeds (shading; m s^{-1}) and vectors at (a and b) 700 hPa, (c and d) 850 hPa, and (e and f) 925 hPa at 0000 UTC 20 May.

The LLJ-A of the good members had a stronger meridional wind component than that of the bad members, and the jet axis of the former was also more northern than that of the latter (Figures 12a and 12c). In contrast, the LLJ-A of the bad members showed a stronger zonal wind component than that of the good members (Figures 12b and 12d). Therefore, a stronger southwesterly low-level jet, with stronger meridional wind and more northern jet axis, can provide convergence in the control area of MCS-A and thus bring more moisture from the south, resulting in more precipitation. These results are consistent with the ESA analysis above.

Similar ESA and composite analyses were conducted for LLJ-B (Figures 13 and 14). The zonal wind was positively correlated with the accumulated precipitation of MCS-B at 850–700 hPa over the west side of the control area ($r \approx 0.54$; Figures 13a and 13b), while the positive correlation for the meridional wind was located south of the control area at 925 hPa (Figure 13f). Such a distribution of correlations suggests that a strong zonal wind at 850–700 hPa over the west of the control area of MCS-B and meridional wind velocity at 925 hPa over the south were significant for heavy rainfall. A strong positive correlation was also found

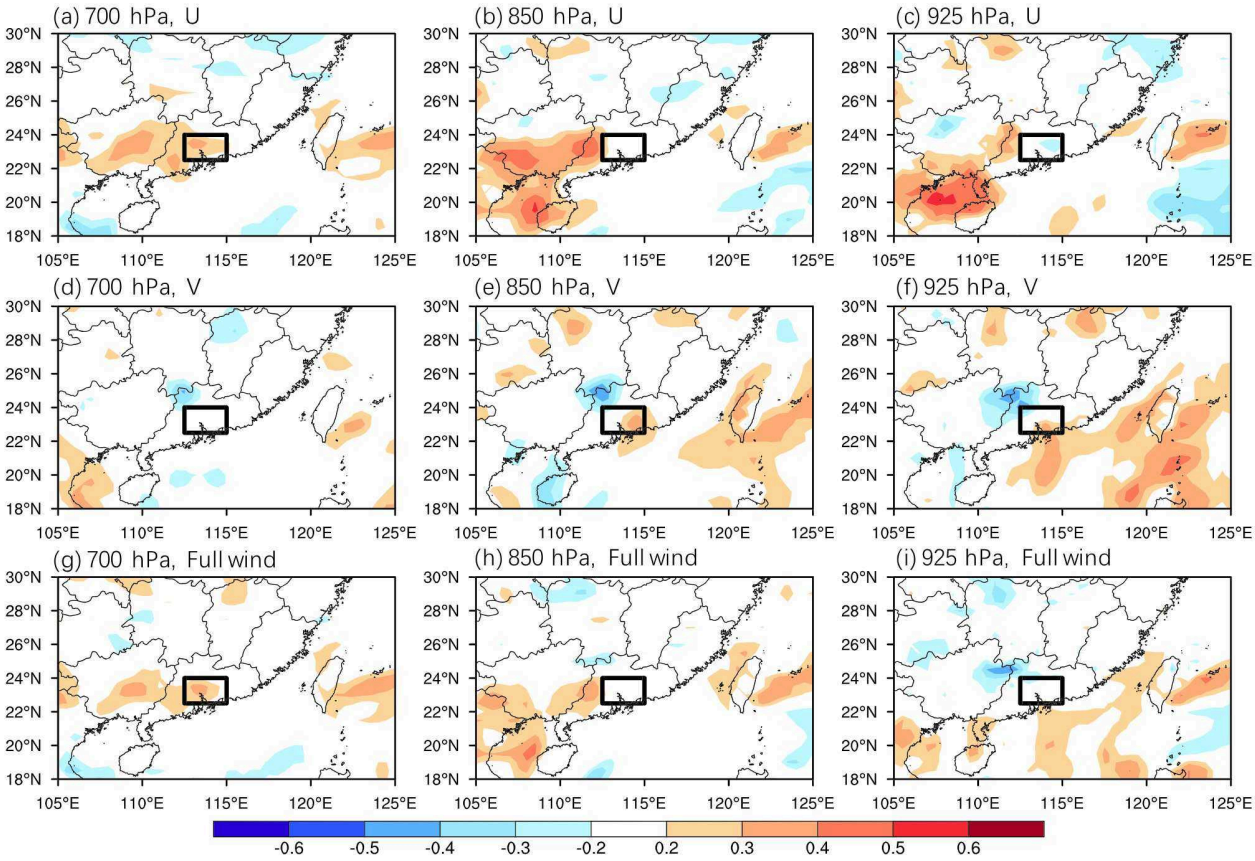

Figure 13. Same as in Figure 11 except for MCS-B.

near 120°E, as the result of strong upstream meridional winds over the South China Sea. A comparison between the full wind speeds of the good and bad members of MCS-B further confirmed the results above (Figure 14). As shown in the good members (Figures 14a, 14c, and 14e), heavy rainfall in the control area of MCS-B was collaboratively affected by both LLJ-A (SLLJ) to the west and LLJ-B (BLJ) to the south. Compared to the bad members, the good members forecasted a stronger SLLJ at 850–700 hPa, with a stronger zonal wind component, and the SLLJ axis tended to be closer to the west side of the control area (Figures 14a–14d). Such conditions were beneficial to the convergence in the control area of MCS-B and thus resulted in more precipitation in MCS B than in MCS-A. In addition, a stronger southerly BLJ at 925 hPa was found over the south of the control area (northern South China Sea) in the good members (Figure 14e) than in the bad members (Figure 14f). Therefore, the heavy rainfall of MCS-B was influenced by both the SLLJ and the BLJ. The wind speed, wind direction, and position of those LLJs were essential to the distribution of precipitation. The divergences derived by the good members of MCS-A and MCS-B are compared in Figure 15. Attributed to the collective effect of SLLJ and BLJ, there was an area of wind convergence in the control area of MCS-B at 850–925 hPa in good members (Figures 15d–15f), which provided favorable conditions for the heavy rainfall of MCS-B. Stronger convergence was found in the control area of MCS-A at 925–700 hPa in the good members of MCS-A (Figures 15a–15c) than in that of MCS-B, whereas no apparent convergence was shown in the control area of MCS-B.

Regarding MCS-C, there were positive correlations between the zonal wind velocity (full wind speed) at 925–700 hPa and accumulated precipitation over the west and southwest of the control area (Figures 16a and 16c). These positive signals imply that increases in the zonal wind velocity and full wind speed over the west of Taiwan Island were related to increased precipitation. This was confirmed by a comparison between the good and bad members (Figures 17 and 18), as the good members forecasted a stronger upstream SLLJ (located in the west of Taiwan Island, marked by black circles in Figures 17c and 17e), with the maximum

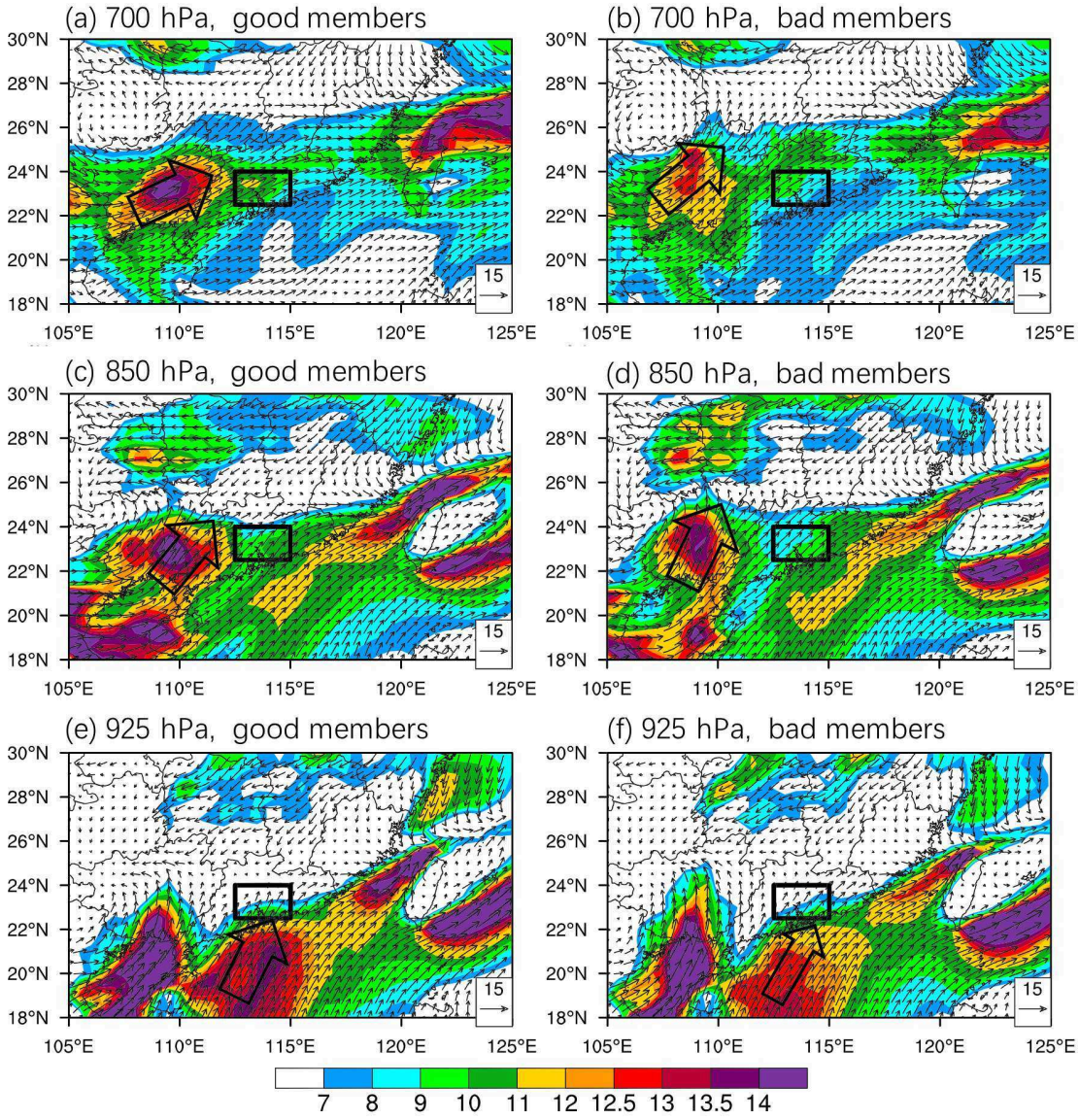

Figure 14. Same as in Figure 12 except for MCS-B.

wind speed over 12 m s^{-1}, and a stronger shear line over the west of Taiwan island (Figure 18). This stronger zonal wind velocity and shear cline could cause stronger convergence over the west of Taiwan Island, especially at 850 hPa (Figure 18c).

5.3. Moisture

Accompanied by LLJs, the moisture that is continuously transported to the control area is essential for heavy rainfall (Higgins et al., 1997; Qian et al., 2004). Therefore, correlations between specific humidity and precipitation were further analyzed to determine the effect of moisture in this section.

With respect to MCS-A and MCS-C, the positive correlations between specific humidity and rainfall covered a large area southwest of their control area (Figures 19a–19c and 19g–19i), which was consistent with the analysis of low-level jets. The result suggests that sufficient transportation of moisture by the synoptic-scale upstream low-level jets is favorable for precipitation in the control area, which was further confirmed by the differences in water vapor flux, $\vec{v}\cdot q$, between good and bad members (Figures 20a–20c and 20g–20i). In the

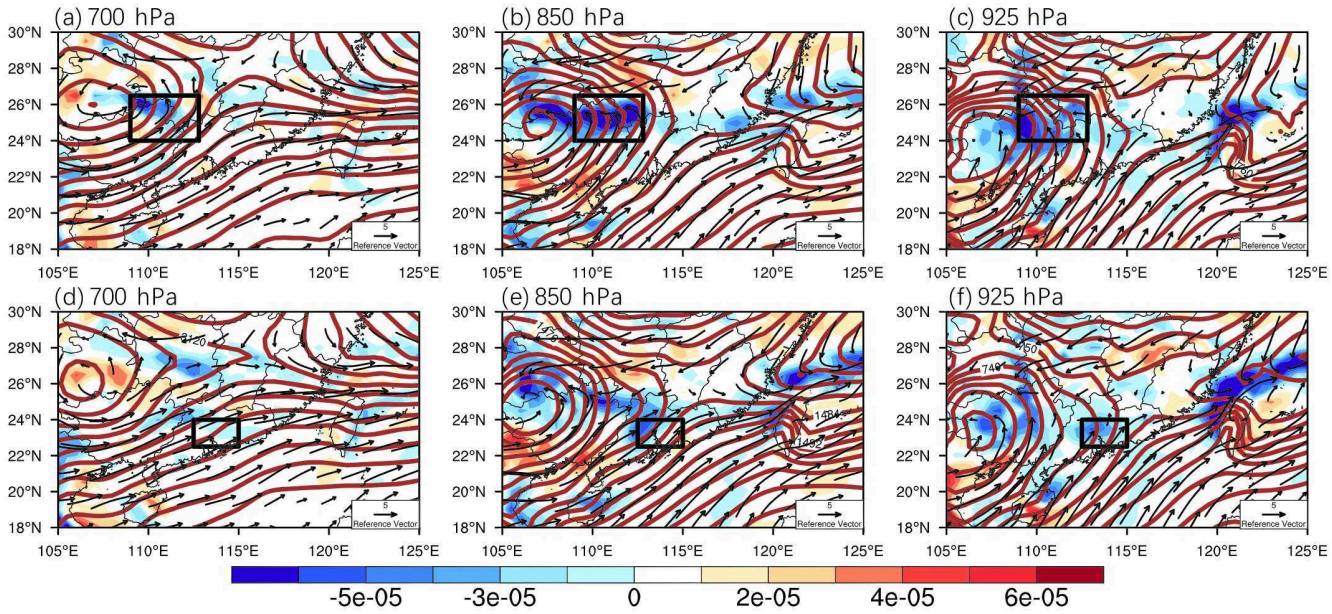

Figure 15. Divergence (shading; s^{-1}), wind vectors, and geopotential height (contour lines; gpm) at (a and d) 700 hPa, (b and e) 850 hPa, and (c and f) 925 hPa averaged from good members of (a–c) MCS-A and (d–f) MCS-B at 0000 UTC 20 May.

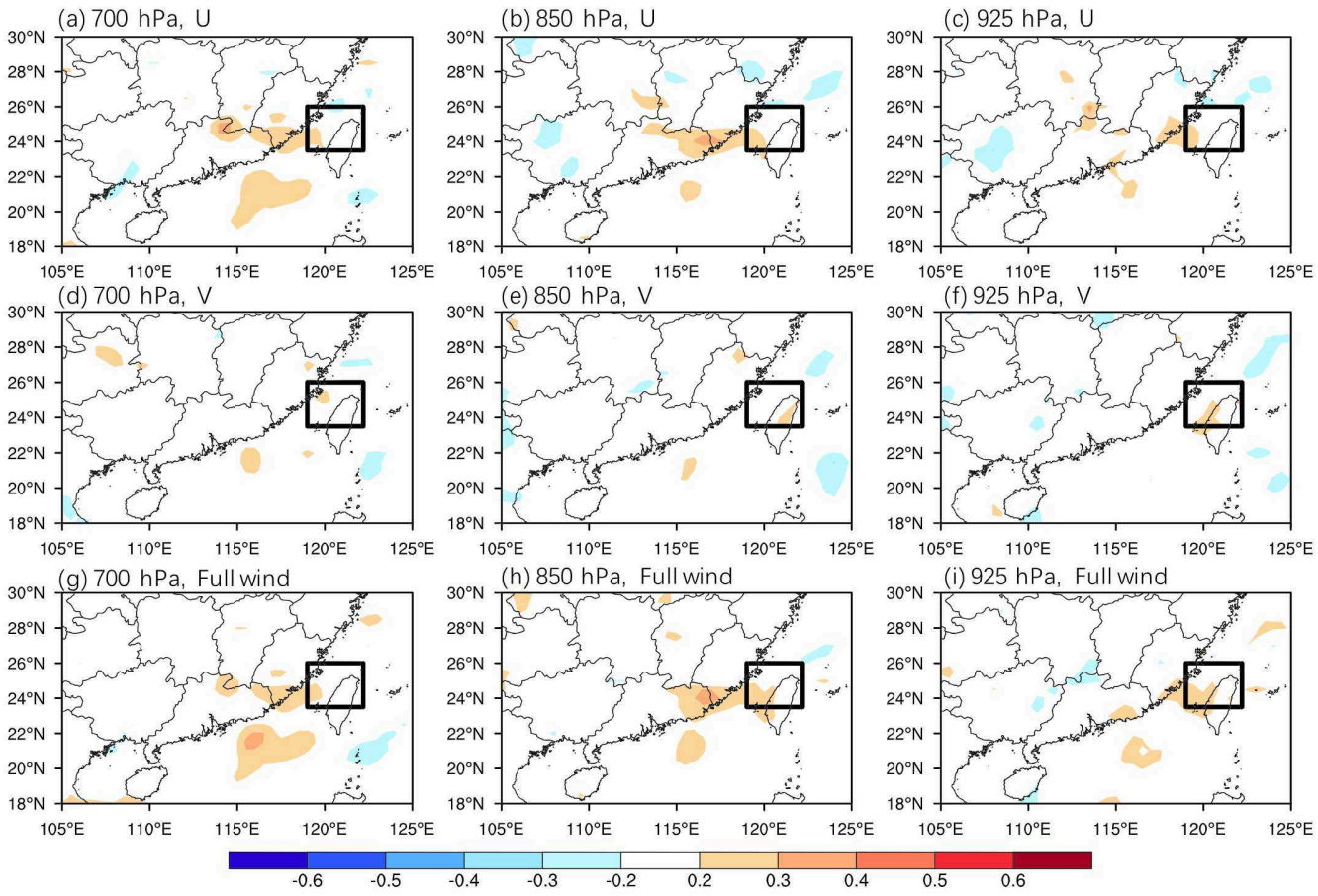

Figure 16. Same as in Figure 11 except for MCS-C.

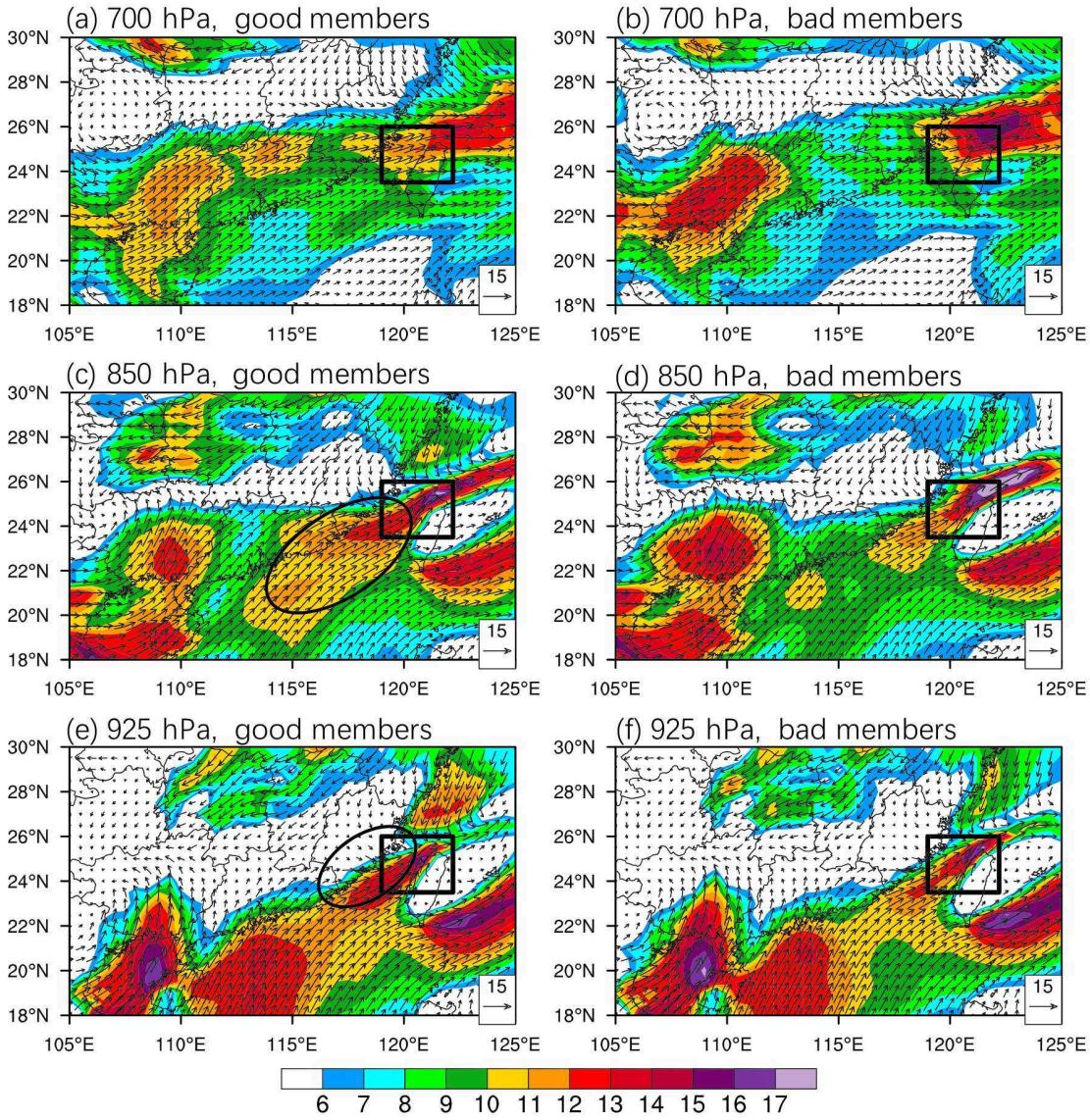

Figure 17. Same as in Figure 12 except for MCS-C.

good members of MCS-A and MCS-C, increased water vapor flux was found upstream of the SLLJs (over the southwest of the control area), indicating that increased moisture transportation to the control area was associated with stronger low-level jets, favoring more precipitation.

The correlations between specific humidity and rainfall of MCS-B (Figures 19d–19f) reflect an apparent positive signal over the southwest of the control area at 850 and 700 hPa. A weak positive signal was found over the south of the control area at 925 hPa. This implies that the sufficient transportation of moisture over the west of the control area at 850–700 hPa and the south of the control area at 925 hPa were beneficial to heavy rainfall in MCS-B. The moisture at 850–700 hPa was more related than that at 925 hPa to precipitation in the control area. According to the composite fields of good and bad members (Figures 20d–20f), the sufficient moisture that favored increased precipitation in MCS-B was transported by two low-level jets, which was highly consistent with the joint effect of the SLLJ and BLJ on the rainfall of MCS-B (mentioned in section 5.2). The differences in the water vapor flux between good members and bad members reached 4 g $(cm{\cdot}hPa{\cdot}s)^{-1}$ at 700–850 hPa, whereas those at 925 hPa were no more than 3 g $(cm{\cdot}hPa{\cdot}s)^{-1}$. Zhang and Meng (2018) found similar characteristics of low-level jets that dominantly influenced moisture transport.

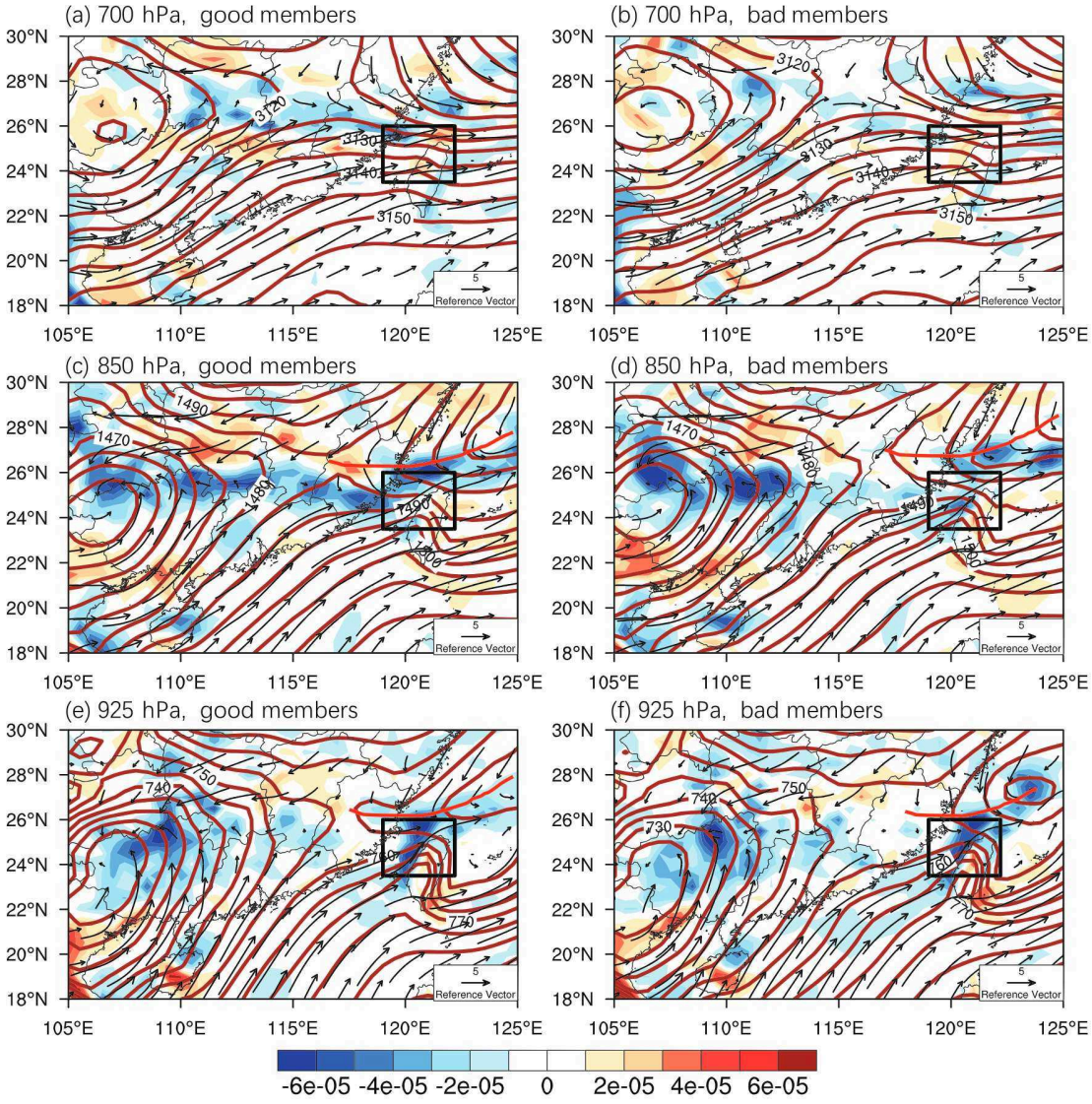

Figure 18. Composite wind fields of (a, c, and e) good members and (b, d, and f) bad members of MCS-C with divergence (shading; s^{-1}), wind vectors, and geopotential height (contour line; gpm) at (a and b) 700 hPa, (c and d) 850 hPa, and (e and f) 925 hPa at 0000 UTC 20 May. The shear lines are marked by red lines.

We also carried out separate analyses of each initialized ensemble. The separate analyses of each initialized ensemble (not shown) were similar to the previously described analyses of 100 ensemble members, except wind velocity is negatively correlated with MCS-B in the correlation between the precipitation of MCS-B and wind velocity in the 50 ensemble members initialized at 0000 UTC 19 May. This difference might be the result of the poor forecast skill of MCS-B in the ensemble set initialized at 0000 UTC 19 May (Figure 5a). The ensemble set initiated at 0000 UTC 19 May almost missed MCS-B, and few members accurately forecasted MCS-B; thus, the ensemble-based analysis did not work for this situation. We will further discuss the predictability of MCS-B through these two ensembles in section 7.

6. Synoptic Fields Beneficial to All Three MCSs

As mentioned in the previous sections, poor performing members of MCS-A trended toward accurately depicting MCS-B. The key factors beneficial to MCS-A were also opposite to those beneficial to MCS-B. We were still interested in the synoptic fields beneficial to all three MCSs, so we further conducted

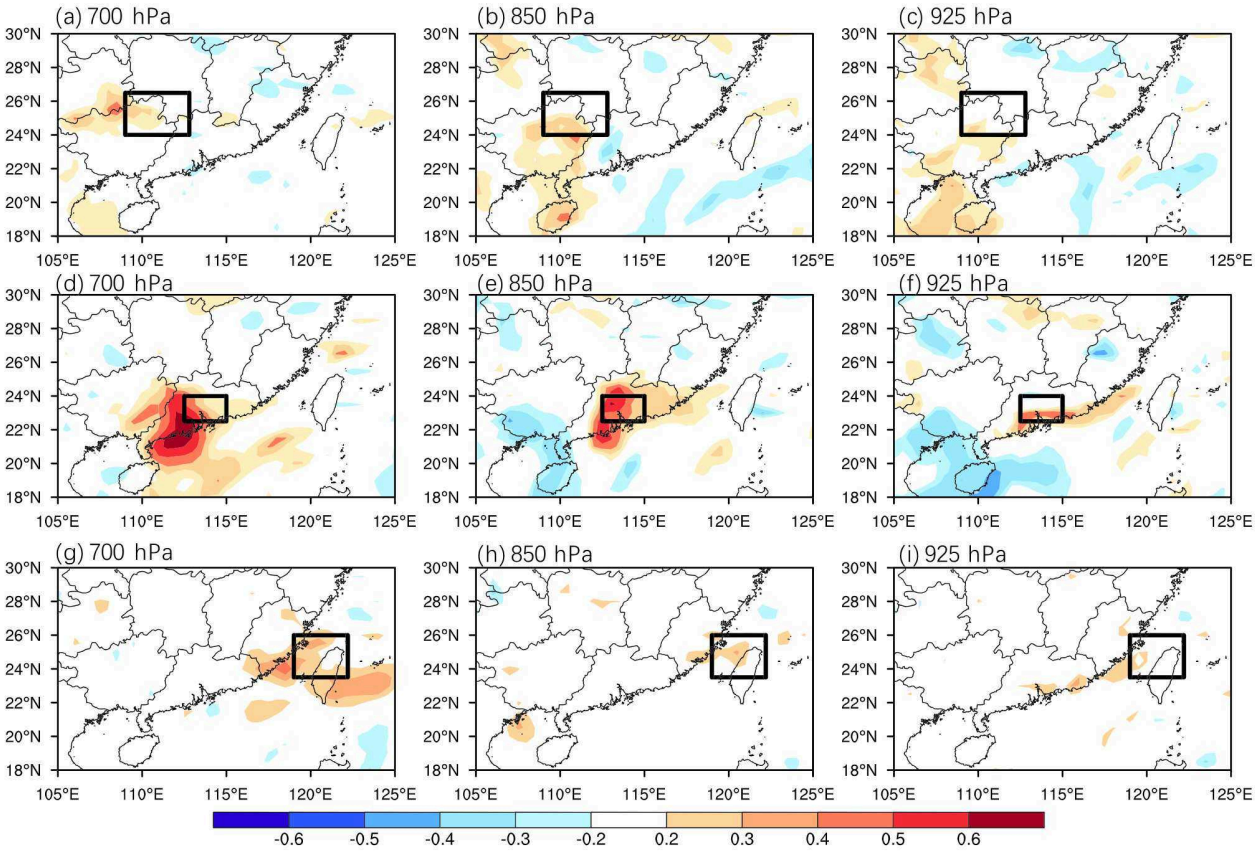

Figure 19. Same as in Figure 8 except with specific humidity.

ensemble-based sensitivity or composite analysis for all three MCSs. Six good members and six bad members of all three MCSs were selected based on the precipitation amount and threat scores. Since many members could not forecast MCS-A and MCS-B well at the same time, the TSs of the good members for all three MCSs were above average but not the highest. Six members (#6, 25, 28, 51, 67, and 73) were chosen as good members (red dots in Figures 6g–6i), whereas six other members (#14, 22, 27, 37, 54, and 75) were chosen as bad members (blue dots in Figures 6g–6i).

The correlation coefficients between the total precipitation of the three MCSs and synoptic factors in 100 ensemble forecast members are presented in Figure 21. Similar to the results of individual MCS, negative correlation signals between rainfall and geopotential height occurred in the control area of MCS-A and MCS-B (Figures 21a–21c), indicating that the low geopotential height in the control region was correlated with increased precipitation in MCS-A and MCS-B. For the correlation coefficients between precipitation and winds (zonal wind velocity, meridional wind velocity, and full wind velocity; Figures 21d–21l), a strong positive signal occurred over the south and southwest of the control area of MCS-A at 850 hPa, indicating that a stronger LLJ-A was correlated with more precipitation. Similarly, the strong positive signal over the south of the control area of MCS-B suggested that a stronger LLJ-B was correlated with more precipitation. Notably, the spread of the ensemble forecast precipitation of MCS-C was relatively small compared to that of MCS-A and MCS-B, as mentioned in section 4 in the manuscript (Figure 6). The correlation signal over the neighboring region of MCS-C was thus relatively weak in the analysis of all three MCSs simultaneously.

Composite geopotential height fields are presented in Figures 21m–21o. Similar to the geopotential height fields from the ERA5 Analysis in Figure 4, good members showed a trough in the control area of MCS-A at 850 hPa and a trough near the control area of MCS-B at 925 hPa (Figures 21m–21o), instead of the northeast-southwest oriented trough at 925–700 hPa shown by the good members of MCS-A (Figures 9a–9c). It is worth mentioning that the good members of all the three MCSs forecasted a LLJ-A featuring

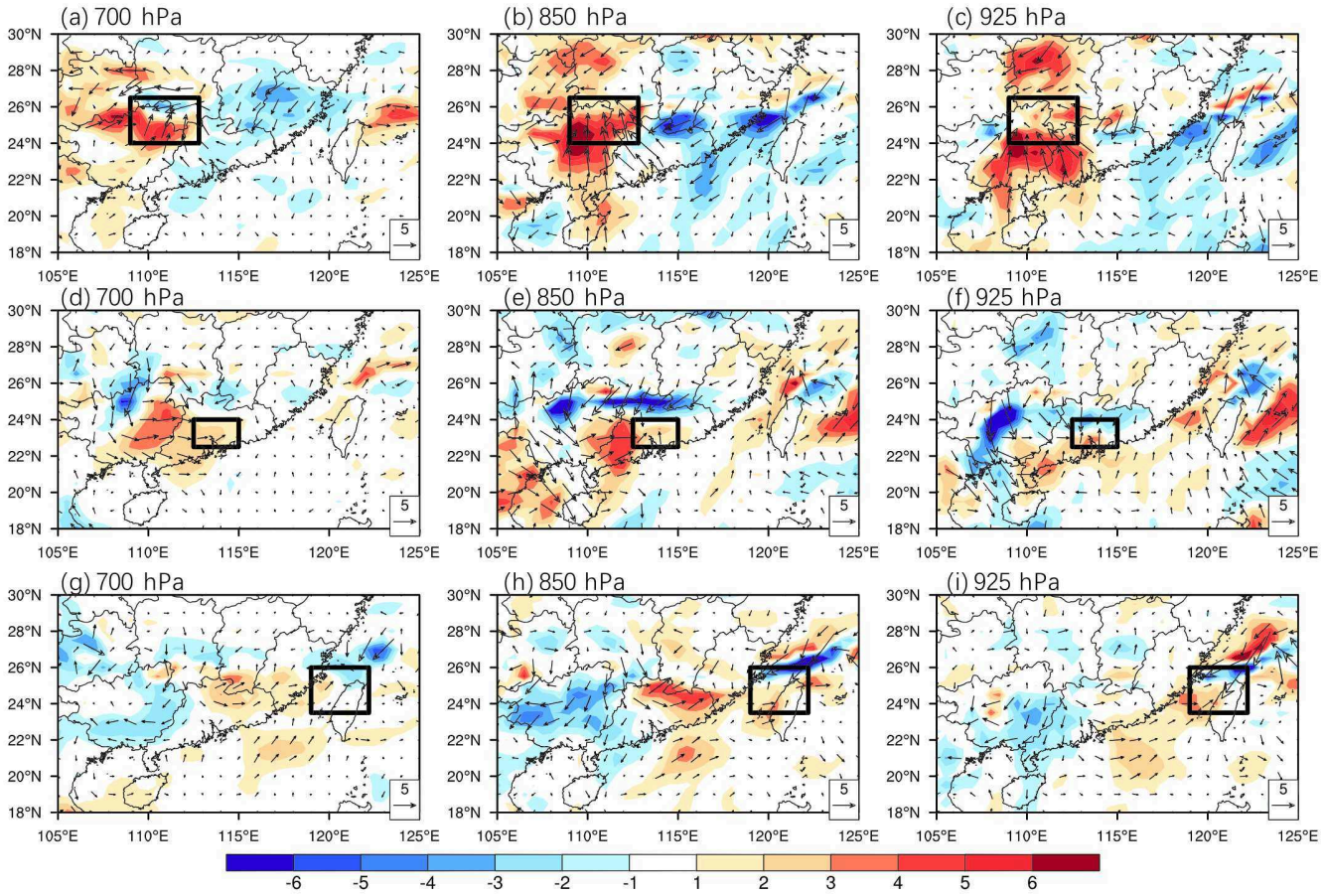

Figure 20. The differences in water the averaged vapor flux (shading and vector; g (cm·hPa·s)$^{-1}$) between good members and bad members of (a–c) MCS-A, (d–f) MCS-B, and (g–i) MCS-C at (a, d, and g) 700 hPa, (b, e, and h) 850 hPa, and (c, f, and i) 925 hPa from the ECWMF ensemble forecasts at 0000 UTC 20 May.

diffluence at the exit of the LLJ-A (Figure 22c), instead of the almost unidirectional LLJ-A forecasted by the good members of MCS-A (or MCS-B). Such diffluence at the exit of LLJ-A was beneficial to both MCS-A and MCS-B. The difference in the wind direction of LLJ-A indeed accounted for the opposite relationship between MCS-A and MCS-B.

7. Discussion on the Predictability of Heavy Rainfall

The ECMWF ensemble forecasts presented the differences in the quantitative forecast skills among the three MCSs (Figure 6). The forecast skill of MCS-B was not as good as that of MCS-A and MCS-C, which might be related to the forecast uncertainty of key factors.

The uncertainty of low-level jets could also strongly influence the rainfall forecast in the control area (Squitieri & Gallus, 2016). To further identify the uncertainties of LLJs, the jet axes of 20 good members and 20 bad members of the three MCSs, chosen based on the forecast precipitation and TSs as before, are plotted by colorful lines in Figure 23. The jet axis length is based on the area over which the wind velocity exceeded 12 m s^{-1} (if the maximum wind velocity was less than 12 m s^{-1}, the axis is not shown). The orientation of the lines is consistent with wind direction across the region with the maximum wind velocity, and the maximum wind velocities of the LLJs are indicated by the color of the lines. As shown in Figure 23, the spread of the three LLJ axes had different features among good and bad members. Considering the axes of LLJ-A at 850 hPa, a higher wind velocity with a stronger meridional wind component and more northern jet axes is found in good members of MCS-A (Figure 23a), while in bad members of MCS-A, the jet axes are more to the south, with a lower velocity and more widespread distribution (Figure 23b). In good

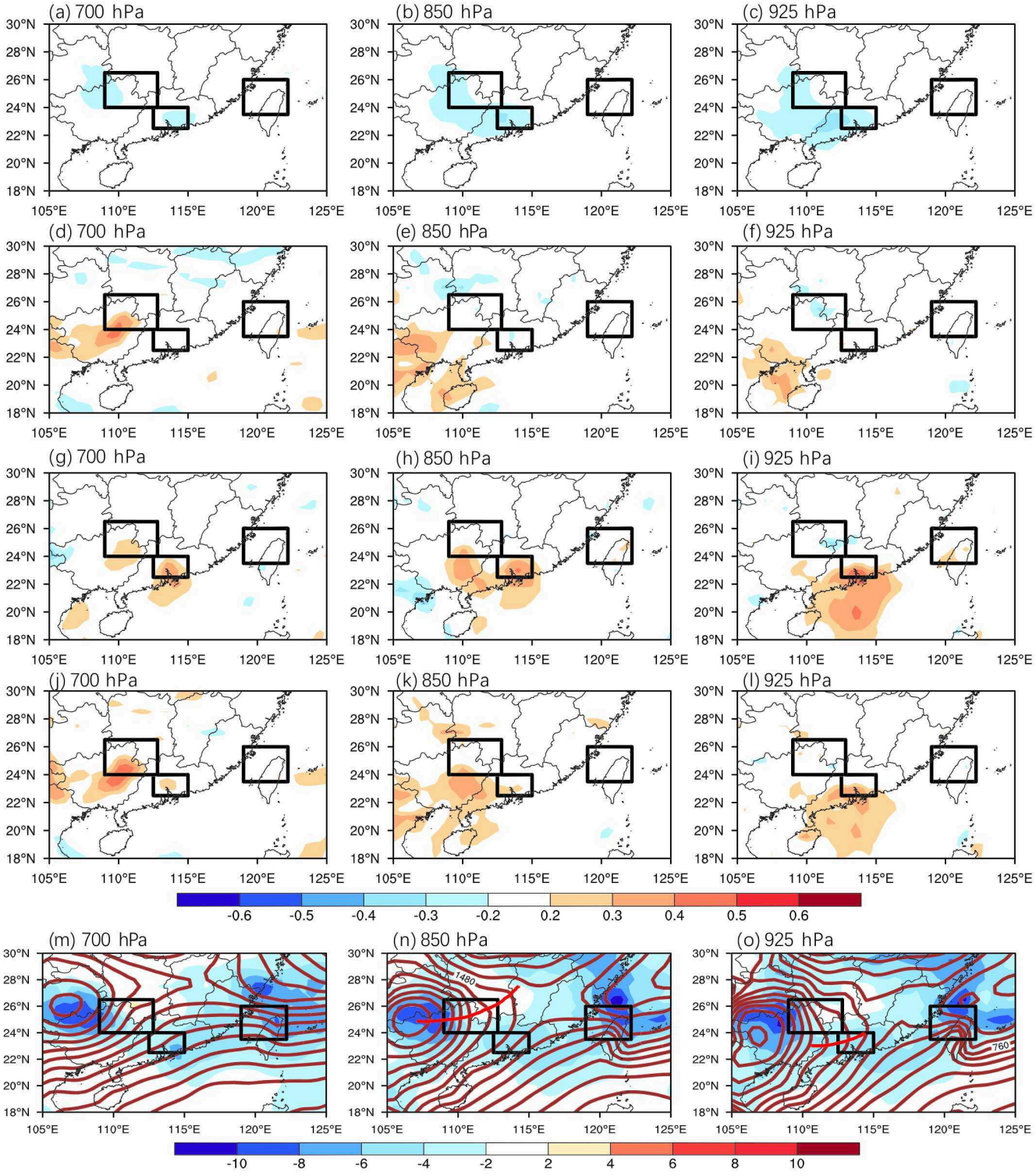

Figure 21. Correlation coefficients (shading) between (a–c) geopotential height, (d–f) zonal wind velocity, (g–i) meridional wind velocity, and (j–l) full wind velocity at (a, d, g, and j) 700 hPa, (b, e, h, and k) 850 hPa, and (c, f, i, and l) 925 hPa at 0000 UTC 20 May and 6-hr accumulated precipitation of the three MCSs during 0000–0600 UTC 20 May. The geopotential heights of good members (contour line; gpm) and the differences between the geopotential heights (shading; gpm) at (m) 700 hPa, (n) 850 hPa, and (o) 925 hPa of good members and bad members. The troughs of the vortex are marked by red lines.

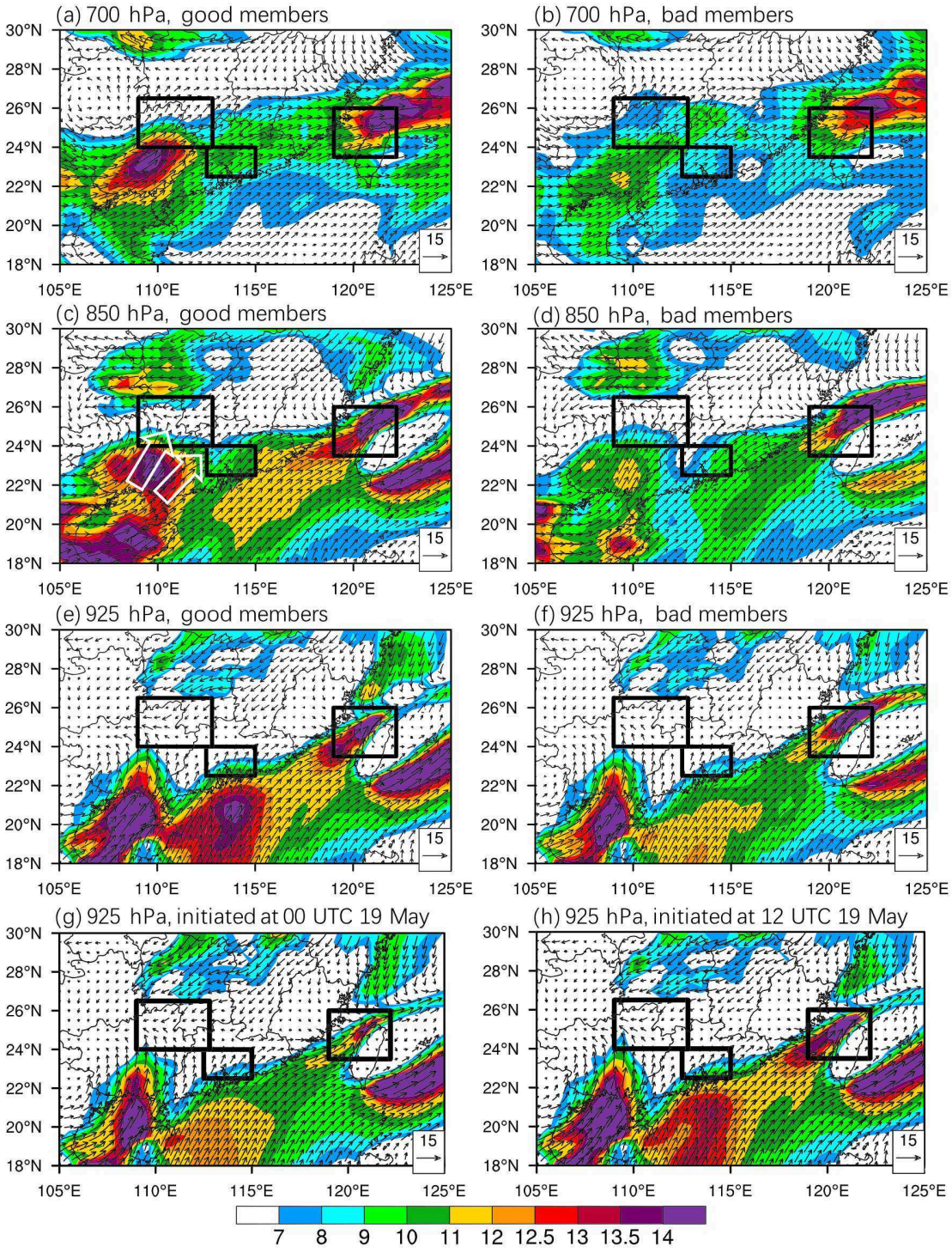

Figure 22. Composite wind fields of (a, c, and e) good members and (b, d, and f) bad members of three MCSs with full wind speeds (shading; m s^{-1}) and vectors at (a and b) 700 hPa, (c and d) 850 hPa, and (e and f) 925 hPa at 0000 UTC 20 May. Ensemble mean wind field at 925 hPa at 0000 UTC 20 May initialized at (g) 0000 UTC 19 May and (h) 1200 UTC 19 May.

members of MCS-B, the axes of LLJ-A at 850 hPa have a stronger zonal wind component and are located more to the south (Figure 23c), but the axes in bad members of MCS-B have a stronger meridional wind component and a more widespread distribution (Figure 23d). These results indicate that the uncertainty

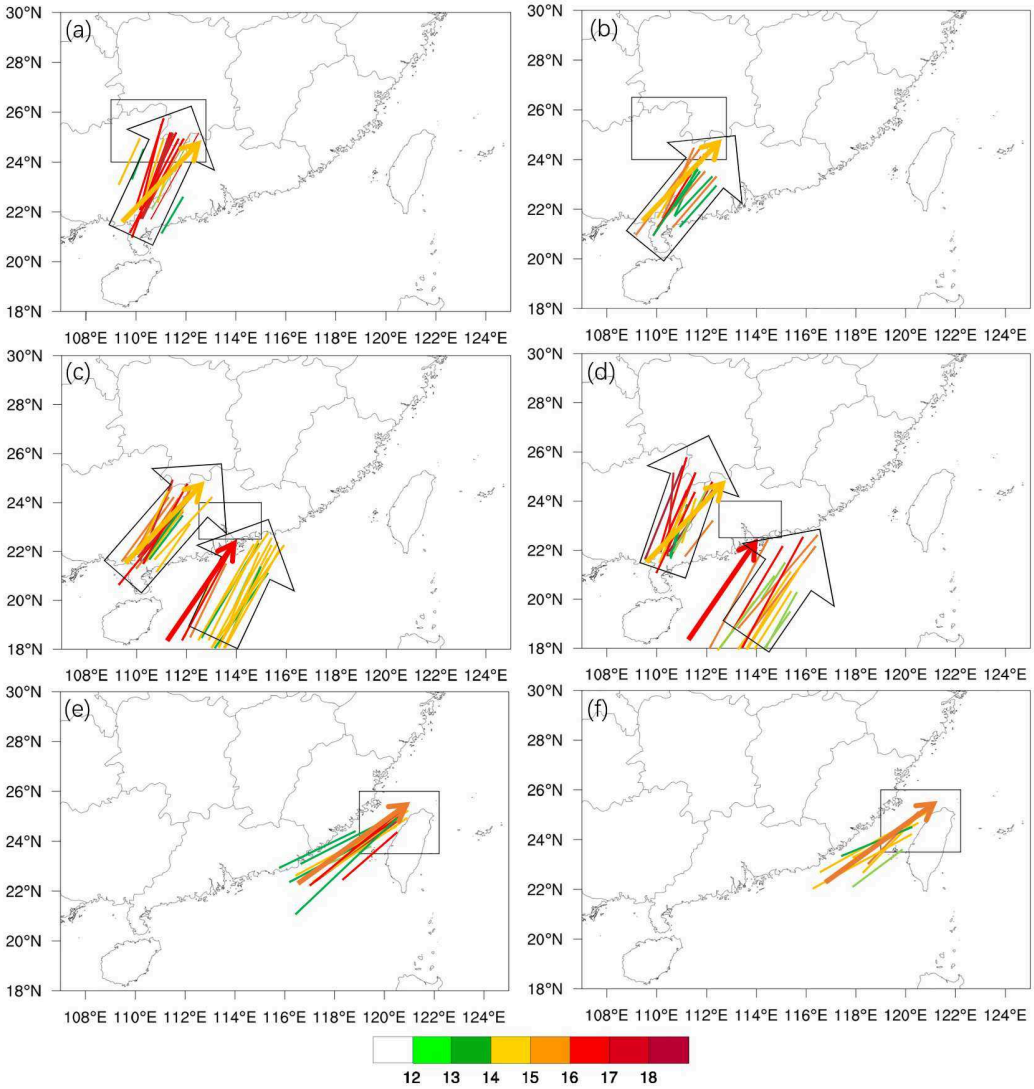

Figure 23. The jet axis of 20 good members and 20 bad members at 0000 UTC 20 May (the line lengths are based on the area over which the wind speed exceeds 12 m s^{-1}, and the color of the lines represents the maximum wind speed). Good and bad members of MCS-A at 850 hPa (LLJ-A) are plotted in (a) and (b), good and bad members of MCS-B at 850 hPa (LLJ-A) and 925 hPa (LLJ-B) are plotted in (c) and (d), and good and bad members of MCS-C at 850 hPa (LLJ-C) are plotted in (g) and (h). The thick lines represent the direction of real LLJs from the ERA5 data set.

of LLJ-A, including uncertainties in the LLJ-A strength, location, and orientation, partly result in the forecast uncertainties of MCS-A and MCS-B. The axes of LLJ-B at 925 hPa of the 20 good members and 20 bad members are also plotted in Figures 20c and 20d. When axes with higher speeds are located more to the west, more moisture is transported to the control area of MCS-B (good members in Figure 23c). However, in bad members, the axes of LLJ-B are located more to the east (Figure 23d), transporting moisture from the South China Sea to the east. The wide distribution of LLJ-A and LLJ-B partly accounts for the difficulty in accurately predicting precipitation (Zhang & Meng, 2018). Furthermore, the complex interaction of the two low-level jets (LLJ-A and LLJ-B) might increase the forecast uncertainty of MCS-B, resulting in the worse quantitative forecast skill of MCS-B. Since the rainfall of MCS-C was influenced by the upstream LLJ, only the upstream axes are plotted. The orientation and location of LLJ-C at 850 hPa of bad members (Figure 23f) were similar to those of good members (Figure 23e), but deviation in the strength was found. The jet axes of real LLJs from the ERA5 data set were also plotted using colorful arrows. Generally, the jet axes of ensemble members were distributed around the jet axes of real LLJs.

According to the ESA of individual MCSs in section 5, the effects of LLJ-A or the vortex on MCS-A and MCS-B were different and opposite. The opposite relationship between the key factors accounted for the opposite relationship between MCS-A and MCS-B. A stronger southwesterly LLJ-A with a stronger meridional (zonal) wind component and more northern (southern) axis produced more precipitation in the corresponding region of MCS-A (MCS-B), and a stronger low-level trough of the southwest vortex in the control area of MCS-A and MCS-B was correlated to more precipitation in MCS-A and MCS-B. MCS-A and MCS-B coexist in reality. According to the ESA of the three MCSs as a whole in section 6, the southwest vortex with a trough in the control area of MCS-A at 850 hPa and a trough near the control region of MCS-B at 925 hPa and LLJ-A featuring diffluence at the exit of LLJ-A were favorable for the coexistence of MCS-A and MCS-B.

The ensemble mean wind fields initialized at 0000 UTC 19 May and 1200 UTC 19 May are presented in Figures 22g–22h. The ensemble set initialized at 0000 UTC 19 May almost missed MCS-B, while the ensemble set initialized at 1200 UTC 19 May captured the occurrence of MCS-B, as mentioned in section 4. The LLJ-B forecasted by the ensemble set initialized at 1200 UTC 19 May was stronger than that initialized at 0000 UTC 19 May. This result was consistent with the previously described results showing that a stronger LLJ-B was correlated with more precipitation in MCS-B.

All ensemble members captured the occurrence of MCS-C but underestimated its rain intensity (Figure 6c). The full wind speed and convergence over the northwest of Taiwan island at 925 hPa in the ERA5 data were stronger than those in ensemble forecasts (not shown). This indicates that the interaction between the low-level wind field and the topography of Taiwan was underestimated by ensemble forecasting, resulting in the magnitude error of MCS-C.

8. Summary and Conclusions

ESA and composite analysis are applied to estimate the key factors of three MCSs coexisting (over southwestern China, the south coast of China, and northern Taiwan simultaneously) in a heavy rainfall event during 19–20 May 2015 and explore their predictability. From the ensemble forecasts of ECMWF, the quantitative forecast skill in MCS-B is generally worse than that in MCS-A and MCS-C, and the forecast accuracies of MCS-A and MCS-B are always opposite. The results of ESA further show that the forecast uncertainty in the rainfall of the three MCSs is closely related to the forecast uncertainty in the relevant vortex/shear line, low-level jets, and moisture transport.

MCS-A was strongly influenced by the southwest vortex and its related LLJ-A, which was a synoptic jet. A strong low-level trough of the southwest vortex located in the control area of MCS-A and strong LLJ-A located more to the north with a strong meridional wind component were correlated with the increased precipitation of MCS-A.

The precipitation of MCS-B was affected not only by the southwest vortex and LLJ-A but also by LLJ-B, which was a boundary layer jet from the South China Sea. A strong low-level trough of the southwest vortex located in the control area of MCS-B was related to increased precipitation in MCS-B. When LLJ-A had a stronger zonal wind component and was located more to the south, it brought more moisture to the control area of MCS-B, favoring the increased precipitation of MCS-B. Furthermore, a stronger LLJ-B at 925 hPa always results in stronger wind convergence in the boundary layer in the control area of MCS-B, which also favors increased precipitation. The low forecast skill of MCS-B might be ascribed to the joint effects of the two low-level jets (LLJ-A and LLJ-B).

According to the ESA of individual MCSs, the effects of the vortex or LLJ-A on MCS-A and MCS-B were different and opposite, but MCS-A and MCS-B coexisted in reality. The southwest vortex with a trough in the control area of MCS-A at 850 hPa and a trough near the control region of MCS-B at 925 hPa and the LLJ-A featuring diffluence at the exit of LLJ-A were favorable for the coexistence of MCS-A and MCS-B.

As for MCS-C, a stronger shear line over the east coast of China and a stronger upstream SLLJ (LLJ-C) with a stronger zonal wind velocity over the west of Taiwan island were related to the increased precipitation of MCS-C. The southwest vortex had little effect on the precipitation of MCS-C.

The quantitative forecast skill of MCS-B was generally worse than that of MCS-A and MCS-C, although most of the ensemble members underestimated the rain intensity of MCS-C. Because of the involvement of

complex factors and the uncertainty of LLJ-B, MCS-B was more sensitive to the initial field than MCS-A and MCS-C. The LLJ-B forecasted by the ensemble set initialized at 1200 UTC 19 May was stronger than that forecasted by the ensemble set initialized at 0000 UTC 19 May, corresponding to the improved forecast skill of the MCS-B in the ensemble set initialized at 1200 UTC 19 May. The magnitude error of MCS-C was attributed to the underestimation of complex effects between the low-level jet and the topography of Taiwan.

In the present study, we confirmed there were differences in the key factors of three coexisting MCSs, and we further found that the complex interaction of SLLJ and BLJ increased the forecast uncertainty of MCS-B, resulting in the worse quantitative forecast skill of MCS-B than of MCS-A and MCS-C. These results are different from the results in previous studies that also showed LLJs were essential in rainfall centers, but without distinguishing between the two types of LLJs (Huang & Luo, 2017; Zhang & Meng, 2018), and that a SLLJ (BLJ) was associated with frontal rainfall (the coastal warm-sector rainfall; Du & Chen, 2018, 2019a). In addition, we also discussed the differences in the predictability of the three MCSs.

The present study suggests that the uncertainty of low-level vortex/shear and low-level jets can strongly influence the forecast capability of the three MCSs. However, questions about the detailed complex interactions between LLJ-A and LLJ-B remain unanswered. Small-scale effects, such as land-sea breezes or cold pools, were not taken into consideration because of the coarse resolution of ECWMF ensemble forecasts. In the future, we plan to conduct high-resolution numerical simulations to further study the detailed structure and evolution of the three MCSs during this rainfall event to better understand the distinctions among their predictability, potentially providing ideas for revising the quantitative forecast.

Acknowledgments

AcknowledgementsThis study was supported by the National Key Research and Development Program of China (grant 2018YFC1507402) and the National Natural Science Foundation of China (grants 41875055, 41861164027, and 41775094), the Fundamental Research Funds for the Central Universities (19lgzd08), and the Young Elite Scientists Sponsorship Program by CAST (2018QNRC001). The ERA-Interim data sets were downloaded from http://apps.ecmwf.int/datasets/data/interim-full-daily/levtype=sfc/, the ERA5 data were available in the Climate Data Store at https://climate.copernicus.eu/climate-reanalysis, and the global ensemble forecast from ECMWF was available at http://apps.ecmwf.int/datasets/data/tigge/levtype=sfc/type=pf/. The authors are thankful to the CPC of NOAA for providing the CMORPH data and thankful to Murong Zhang for her method and discussion.

References

Bednarczyk, C. N., & Ancell, B. C. (2015). Ensemble sensitivity analysis applied to a southern plains convective event. *Monthly Weather Review*, *143*(1), 230–249. https://doi.org/10.1175/MWR-D-13-00321.1

Bei, N., & Zhang, F. (2007). Impacts of initial condition errors on mesoscale predictability of heavy precipitation along the Mei-Yu front of China. *Quarterly Journal of the Royal Meteorological Society*, *133*(622), 83–99. https://doi.org/10.1002/qj.20

Blackadar, A. K. (1957). Boundary layer wind maxima and their significance for the growth of nocturnal inversions. *Bulletin of the American Meteorological Society*, *38*, 283–290.

Catto, J. L., Madonna, E., Joos, H., Rudeva, I., & Simmonds, I. (2015). Global relationship between fronts and warm conveyor belts and the impact on extreme precipitation*. *Journal of Climate*, *28*(21), 8411–8429. https://doi.org/10.1175/JCLI-D-15-0171.1

Chen, G., Lan, R., Zeng, W., Pan, H., & Li, W. (2018). Diurnal variations of rainfall in surface and satellite observations at the monsoon coast (South China). *Journal of Climate*, *31*(5), 1703–1724. https://doi.org/10.1175/JCLI-D-17-0373.1

Chen, X., Zhang, F., & Zhao, K. (2016). Diurnal variations of land-sea breeze and its related precipitation over South China. *Journal of the Atmospheric Sciences*, *73*(12), 4793–4815. https://doi.org/10.1175/JAS-D-16-0106.1

Chen, X., Zhao, K., Xue, M., Zhou, B., Huang, X., & Xu, W. (2015). Radar-observed diurnal cycle and propagation of convection over the Pearl River Delta during Mei-Yu season. *Journal of Geophysical Research: Atmospheres*, *120*, 12,557–12,575. https://doi.org/10.1002/2015JD023872

Du, Y., & Chen, G. X. (2018). Heavy rainfall associated with double low-level jets over southern China. Part I: Ensemble-based analysis. *Monthly Weather Review*, *146*, 3827–3844. https://doi.org/10.1175/MWR-D-18-0101.1

Du, Y., & Chen, G. X. (2019a). Heavy rainfalls associated with double low-level jets over southern China. Part II: Convection initiation. *Monthly Weather Review*, *147*, 543–565. https://doi.org/10.1175/MWR-D-18-0102.1

Du, Y., & Chen, G. X. (2019b). Climatology of low-level jets and their impact on rainfall over southern China during the early-summer rainy season. *Journal of Climate*, *32*(24), 8813–8833. https://doi.org/10.1175/JCLI-D-19-0306.1

Du, Y., & Rotunno, R. (2014). A Simple Analytical Model of the Nocturnal Low-level Jet over the Great Plains of the United State. *Journal of the Atmospheric Sciences*, *71*(10), 3674–3683. https://doi.org/10.1175/JAS-D-14-0060.1

Du, Y., & Rotunno, R. (2018). Diurnal cycle of rainfall and winds near the south coast of China. *Journal of the Atmospheric Sciences*, *75*, 2065–2082. https://doi.org/10.1175/JAS-D-17-0397.1

Du, Y., Zhang, Q., & Ying, Y. (2012). Characteristics of low-level jets in shanghai during the 2008-2009 warm seasons as inferred from wind profiler radar data. *Journal of the Meteorological Society of Japan*, *90*(6), 891–903. https://doi.org/10.2151/jmsj.2012-603

Du, Y., Zhang, Q., Chen, Y., et al. (2014). Numerical Simulations of Spatial Distributions and Diurnal Variations of Low-Level Jets in China during Early Summer. *Journal of Climate*, *27*(15):5747–5767. https://doi.org/10.1175/JCLI-D-13-00571.1

Gopalakrishnan, S. G., Goldenberg, S., Quirino, T., Zhang, X., Marks, F. Jr., Yeh, K. S., et al. (2011). Toward improving high-resolution numerical hurricane forecasting: Influence of model horizontal grid resolution, initialization, and physics. *Weather and Forecasting*, *27*(3), 647–666. https://doi.org/10.1175/WAF-D-11-00055.1

Hakim, G. J., & Torn, R. D. (2008). Ensemble synoptic analysis. Synoptic–dynamic meteorology and weather analysis and forecasting: A tribute to Fred Sanders (no. 55, pp. 147–161). American Meteorological Society. https://doi.org/10.1007/978-0-933876-68-2_7

Higgins, R. W., Yao, Y., Yarosh, E. S., Janowiak, J. E., & Mo, K. C. (1997). Influence of the Great Plains low-level jet on summertime precipitation and moisture transport over the Central United States. *Journal of Climate*, *10*(3), 481–507. https://doi.org/10.1175/1520-0442(1997)010<0481:IOTGPL>2.0.CO;2

Hill, A., Weiss, C. C., & Ancell, C. B. (2016). Ensemble sensitivity analysis for mesoscale forecasts of dryline convection initiation. *Monthly Weather Review*, *144*(11), 4161–4182. https://doi.org/10.1175/MWR-D-15-0338.1

Holton, J. R. (1967). The diurnal boundary layer wind oscillation above sloping terrain. *Tellus*, *19*, 199–205. https://doi.org/10.1111/j.2153-3490.1967.tb01473.x

Huang, L., & Luo, Y. (2017). Evaluation of quantitative precipitation forecasts by TIGGE ensembles for south China during the presummer rainy season. *Journal of Geophysical Research: Atmospheres*, *122*, 8494–8516. https://doi.org/10.1002/2017JD026512

Huang, L., Luo, Y., & Zhang, D.-L. (2018). The relationship between anomalous presummer extreme rainfall over the South China and synoptic disturbances. *Journal of Geophysical Research: Atmospheres*, *123*, 3395–3413. https://doi.org/10.1002/2017JD028106

Jing, L., Lu, H., Wang, H., Zhu, M., & Kou, Z. (2004). A mesoscale analysis of heavy rain caused by frontal and topographical heterogeneities on Taiwan island. *Advances in Atmospheric Sciences*, *21*(6), 909–922. https://doi.org/10.1007/BF02915593

Joyce, R. J., Janowiak, J. E., Arkin, P. A., & Xie, P. (2004). CMORPH: A method that produces global precipitation estimates from passive microwave and infrared data at high spatial and temporal resolution. *Journal of Hydrometeorology*, *5*(3), 287–296. https://doi.org/10.1175/1525-7541(2004)005<0487:CAMTPG>2.0.CO;2

Kumar, P., Ojha, S. P., Singh, R., Kishtawal, C. M., & Pal, P. K. (2015). Performance of weather research and forecasting model with variable horizontal resolution. *Theoretical and Applied Climatology*, *126*(3-4), 705–713. https://doi.org/10.1007/s00704-015-1607-7

Kuo, Y., & Chen, T. (1990). The Taiwan Area Mesoscale Experiment (TAMEX): An overview. *Bulletin of the American Meteorological Society*, *71*(1990), 488–503. https://doi.org/10.1175/1520-0477(1990)071<0488:TTAMEA>2.0.CO;2

Liu, X., Luo, Y., Guan, Z., & Zhang, D.-L. (2018). An extreme rainfall event in coastal South China during SCMREX-2014: Formation and roles of rainband and echo trainings. *Journal of Geophysical Research: Atmospheres*, *123*, 9256–9278. https://doi.org/10.1029/2018JD028418

Luo, Y., Wang, H., Zhang, R., Qian, W., & Luo, Z. (2013). Comparison of rainfall characteristics and convective properties of monsoon precipitation systems over south China and the Yangtze and Huai river basin. *Journal of Climate*, *26*, 110–132. https://doi.org/10.1175/JCLI-D-12-00100.1

Luo, Y., Wu, M., Ren, F., Li, J., & Wong, W. K. (2016). Synoptic situations of extreme hourly precipitation over china. *Journal of Climate*, *29*(24), 8703–8719. https://doi.org/10.1175/JCLI-D-16-0057.1

Luo, Y., Zhang, R., Wan, Q., Wang, B., Wong, W. K., Hu, Z., et al. (2017). The Southern China Monsoon Rainfall Experiment (SCMREX). *Bulletin of the American Meteorological Society*, *98*(5), 999–1013. http://doi.org/10.1175/BAMS-D-15-00235.1

Lynch, S. L., & Schumacher, R. S. (2014). Ensemble-based analysis of the may 2010 extreme rainfall in Tennessee and Kentucky. *Monthly Weather Review*, *142*(1), 222–239. https://doi.org/10.1175/MWR-D-13-00020.1

Monaghan, A. J., Rife, D. L., Pinto, J. O., Davis, C. A., & Hannan, J. R. (2010). Global precipitation extremes associated with diurnally varying low-level jets. *Journal of Climate*, *23*(19), 5065–5084. https://doi.org/10.1175/2010JCLI3515.1

Park, Y. Y., Buizza, R., & Leutbecher, M. (2008). TIGGE: Preliminary results on comparing and combining ensembles. *Quarterly Journal of the Royal Meteorological Society*, *134*(637), 2029–2050. https://doi.org/10.1002/qj.334

Qian, J. H., Tao, W. K., & Lau, K. M. (2004). Mechanisms for torrential rain associated with the Mei-Yu development during SCSMEX 1998. *Monthly Weather Review*, *132*(1), 3–27. https://doi.org/10.1175/1520-0493(2004)132<0003:MFTRAW>2.0.CO;2

Schaefer, T. (1990). The critical success index as an indicator of warning skill. *Weather and Forecasting*, *5*(4), 570–575. https://doi.org/10.1175/1520-0434(1990)005<0570:TCSIAA>2.0.CO;2

Schumacher, R. S. (2011). Ensemble-based analysis of factors leading to the development of a multiday warm-season heavy rain event*. *Monthly Weather Review*, *139*(139), 3016–3035. https://doi.org/10.1175/MWR-D-10-05022.1

Squitieri, B. J., & Gallus, W. A. J. (2016). WRF forecasts of great plains nocturnal low-level jet-driven MCSs. Part I: Correlation between low-level jet forecast accuracy and MCS precipitation forecast skill. *Weather and Forecasting*, *31*(4), 1301–1323. https://doi.org/10.1175/WAF-D-15-0151.1

Torn, D., & Romine, G. (2015). Sensitivity of central Oklahoma convection forecasts to upstream potential vorticity anomalies during two strongly forced cases during mpex. *Monthly Weather Review*, *143*, 4064–4087. https://doi.org/10.1175/MWR-D-15-0085.1

Torn, R. D., Romine, G. S., & Galarneau, T. J. (2017). Sensitivity of dryline convection forecasts to upstream forecast errors for two weakly forced MPEX cases. *Monthly Weather Review*, *145*, 1831–1852. https://doi.org/10.1175/MWR-D-16-0457.1

Wang, C. (2014). On the calculation and correction of equitable threat score for model quantitative precipitation forecasts for small verification areas: The example of Taiwan. *Weather and Forecasting*, *29*(4), 788–798. https://doi.org/10.1175/waf-d-13-00087.1

Wang, H., Luo, Y., & Jou, B. J.-D. (2014). Initiation, maintenance, and properties of convection in an extreme rainfall event during SCMREX: Observational analysis. *Journal of Geophysical Research: Atmospheres*, *119*, 13,206–13,232. https://doi.org/10.1002/2014JD022339

Wu, M., & Luo, Y. (2016). Mesoscale observational analysis of lifting mechanism of a warm-sector convective system producing the maximal daily precipitation in China mainland during pre-summer rainy season of 2015. *Journal of Meteorological Research*, *30*(5), 719–736. https://doi.org/10.1007/s13351-016-6089-8

Wu, M., Luo, Y., Chen, F., & Wong, W.-K. (2019). Observed link of extreme hourly precipitation changes to urbanization over coastal South China. *Journal of Applied Meteorology and Climatology*, *58*, 1799–1819.

Yu, H., & Meng, Z. (2016). Key synoptic-scale features influencing the high-impact heavy rainfall in Beijing, China, on 21 July 2012. *Tellus A: Dynamic Meteorology and Oceanography*, *68*(1), 31,045. https://doi.org/10.3402/tellusa.v68.31045

Zhang, M., & Meng, Z. (2018). Impact of synoptic-scale factors on rainfall forecast in different stages of a persistent heavy rainfall event in South China. *Journal of Geophysical Research: Atmospheres*, *123*, 3574–3593. https://doi.org/10.1002/2017JD028155

Zhang, M., & Meng, Z. (2019). Warm-sector heavy rainfall in southern China and its WRF simulation evaluation: A low-level-jet perspective. *Monthly Weather Review*, *147*, 4461–4480. https://doi.org/10.1175/MWR-D-19-0110.1

Zhang, Q., Lau, K., Kuo, Y., & Chen, S. J. (2003). A numerical study of a mesoscale convective system over the Taiwan strait. *Monthly Weather Review*, *131*(6), 1150. https://doi.org/10.1175/1520-0493(2003)131<1150:ANSOAM>2.0.CO;2

Zhou, X., Xue, J., Tao, Z., Zhao, S., Yi, Q., & Su, B. (2003). *Heavy Rainfall Experiment in South China during Pre-summer Rainy Season (HUAMEX), 1998*, (p. 220). Beijing: China Meteorological Press. (in Chinese)

Zhu, K., & Xue, M. (2016). Evaluation of WRF-based convection-permitting multi-physics ensemble forecasts over China for an extreme rainfall event on 21 July 2012 in Beijing. *Advances in Atmospheric Sciences*, *33*(11), 1240–1258. https://doi.org/10.1007/s00376-016-6202-z